Chemical Engineering Journal 520 (2025) 165799

Contents lists available at ScienceDirect

Chemical Engineering Journal

journal homepage: www.elsevier.com/locate/cej

Revealing the "double-layer ionic monotonic adsorption" electrochemical ion storage mechanism of nano-confined porous carbon

Gaojie Li [a,1], Xinbo Guo [a], Yu Liu [a,*], Jianguo Sun [c], Hang Yang [b], Yang Zheng [a], Xuming Zhang [a], Paul K. Chu [d,e,f], Guanjie He [b,*], Biao Gao [a,*]

[a] The State Key Laboratory of Advanced Refractories, Wuhan University of Science and Technology, Wuhan 430081, China
[b] Christopher Ingold Laboratory, Department of Chemistry, University College London, 20 Gordon Street, London WC1H 0AJ, UK
[c] Department of Materials Science and Engineering, National University of Singapore, Singapore 117574, Singapore
[d] Department of Physics, City University of Hong Kong, Tat Chee Avenue, Hong Kong, China
[e] Department of Materials Science and Engineering, City University of Hong Kong, Tat Chee Avenue, Hong Kong, China
[f] Department of Biomedical Engineering, City University of Hong Kong, Tat Chee Avenue, Hong Kong, China

ARTICLE INFO

Keywords:
Molten salt
Nano-confined porous carbon
High energy density supercapacitors
Double-layer ionic monotonic adsorption

ABSTRACT

High voltage carbon-based capacitors used organic electrolytes show great potential due to high energy density, wide operating voltage, and long cycle stability. However, oxygen groups in carbon-based materials will undergo oxygen evolution reaction at high potential, leading to failure of the electrode material and triggering the decline of the capacitor. In addition, the ion storage mechanism of carbon-based materials in high voltage ionic liquids is unclear. Herein, we present a scalable method to synthesize three-dimensional porous flower-like carbon (3DPFC) composed of interconnected carbon sheets, highly interconnected pores, large specific surface area, low oxygen content from coconut shells using a simple bicarbonate activation method. Furthermore, combining *in situ* spectroscopy and theoretical calculations, a new "double-layer ionic monotonic adsorption" ion storage mechanism is revealed to be different from the conventional one, and the relationship between the pore structure and the ion storage behavior has been sublimely understood. As a result, the symmetrical supercapacitors using 3DPFC deliver an ultrahigh energy density (109 Wh kg^{-1}) and high-power density (71 kW kg^{-1}), retaining 94.1 % after 10,000 cycles at 10 A g^{-1}. This study highlights the scalable production of high-capacity and low-oxygen-content carbon materials and offers insights into ion storage mechanisms for developing high-energy-density supercapacitors.

1. Introduction

Supercapacitors have deemed to as one of the most essential energy-storage devices due to their intrinsic characteristics of fast charge-discharge rate and long lifespan [1–4]. Carbon-based materials are currently selected as electrode materials for supercapacitors due to their large surface area, high chemical stability and low cost [5–7]. However, the insufficient stability of carbon materials under high-voltage conditions and the poor ion diffusion kinetics in carbon pores have greatly restricted the large-scale application of high-energy-density carbon-based supercapacitors [8–10]. Increasing voltage window of supercapacitors by using organic and ionic liquid electrolytes (2–4.4 V) has been regarded as an effective strategy for achieving high energy density carbon-based supercapacitors [11]. Among them, [EMIM][BF_4] with moderate ion size of 1.3 nm, high operating voltage, and high safety, has been emerged as a wide used electrolyte for high energy capacitors [12]. Chen et al. used organic electrolyte instead of aqueous electrolyte to increase the capacitor voltage window from 1.0 V to 2.7 V, and hierarchical porous carbon with 3D connected pores obtain a high energy density of 33.9 Wh kg^{-1} in [EMIM][BF_4]/PC electrolyte [13]. Liu et al. designed a 3D porous carbon with high SSA and dense and small pores by the HTS-KOH activation process, which deliver a high energy density of 25 Wh kg^{-1} in the [EMIM][BF_4] electrolyte [14]. Owing to a high oxygen content, most 3D porous carbon often suffers from oxygen evolution under high-voltage environment, leading to a poor cycling stability and limit limited power density. Moreover, previous studies

* Corresponding authors.
E-mail addresses: liuyu_lab@163.com (Y. Liu), g.he@ucl.ac.uk (G. He), gaobiao@wust.edu.cn (B. Gao).
[1] These authors contributed equally to this work

https://doi.org/10.1016/j.cej.2025.165799
Received 21 April 2025; Received in revised form 19 June 2025; Accepted 7 July 2025
Available online 8 July 2025

have shown that 3D porous carbon can effectively improve its capacitive properties in [EMIM][BF_4] electrolyte [15], however, the structure-activity relationship between pore size and the ion storage mechanism in carbon materials remains unclear. Specifically, in [EMIM][BF_4] ionic liquids, ions are held together by a strong electrostatic Coulomb forces, creating a Coulombic ordered structure rather than a solvation shell [16,17]. In the standing time, when the pore size is >1.3 nm, anions and cations alternately adsorb onto the carbon wall surface due to the Coulombic ordering (Scheme 1a) [18]. As the pore size narrows from 1.3 to 0.9 nm, the interaction between the carbon wall and ions gradually strengthens, disrupting the Coulombic ordering and leading to a both carbon wall adsorption and Coulombic ordering controlled random dispersion of ions within the pores (Scheme 1b). For the pore size under 0.9 nm, the Coulombic ordering and the larger ion radius of $[EMIM]^+$ (0.76 nm) will impede ion diffusion (Scheme 1c) [16]. When charging the electrode (negative), an overshielding effect occurs in pores larger than 1.3 nm, resulting in the breakdown of the double layer (Scheme 1d). This allows excess $[EMIM]^+$ to accumulate on the surface, with $[BF_4]^-$ neutralizing the excess positive charge in the sublayer. For pores smaller than 1.3 nm, the interaction between the double-layer carbon wall and $[EMIM]^+$ is capable of inhibiting the overshielding effect, promoting the parallel adsorption of $[EMIM]^+$ onto the carbon wall surface (Scheme 1e–f). This enhances charges storage and promotes ion diffusion. In pores under 0.9 nm, although cations can adsorb in a single-layer parallel manner on the carbon wall surface, the optimal carbon pore storage utilization ratio and high ion diffusion kinetics are not achieved (Scheme 1f). In the 0.9 to 1.3 nm range, the double-layer parallel adsorption of $[EMIM]^+$ on the carbon walls surface may offer the optimum balance for high storage density and rapid dynamics (Scheme 1e). Consequently, Consequently, producing large-scale carbon materials with high oxidation resistance, excellent electrical conductivity, and a well-designed 3D porous structure remains a significant challenge. Achieving these qualities, along with understanding the ion storage mechanism, is key to advancing the performance of these materials.

Herein, we present a straightforward double carbonate activation method to convert bio-waste coconut shells into 3DPFC with ultrathin interconnected carbon sheets, 3D connected pores, suitable pore size distribution (1.2 nm) and low oxygen content (4.8 %). During activation, carbonate undergoes a reduction reaction to produce alkali metals that subsequently catalyze the polymerization of graphite microcrystals from biomass decomposition, leading to the formation of ultrathin and highly graphitized carbon sheets with a large specific surface area and low oxygen content enabling a rich active sites and perfect conductivity. Such an 3D flower-like structure with a confined pore size of 1.2 nm offers an ideal pore-platform (0.9–1.3 nm) to form a “double-layer ionic monotonic adsorption” of $[EMIM]^+$ on the carbon pores, which enable the optimum balance for high storage density and rapid dynamics. As a result, the 3DPFC exhibit both high energy density of 109 Wh kg^{-1} in and ultrafast power density of 71 kW kg^{-1} in [EMIM][BF_4] electrolytes.

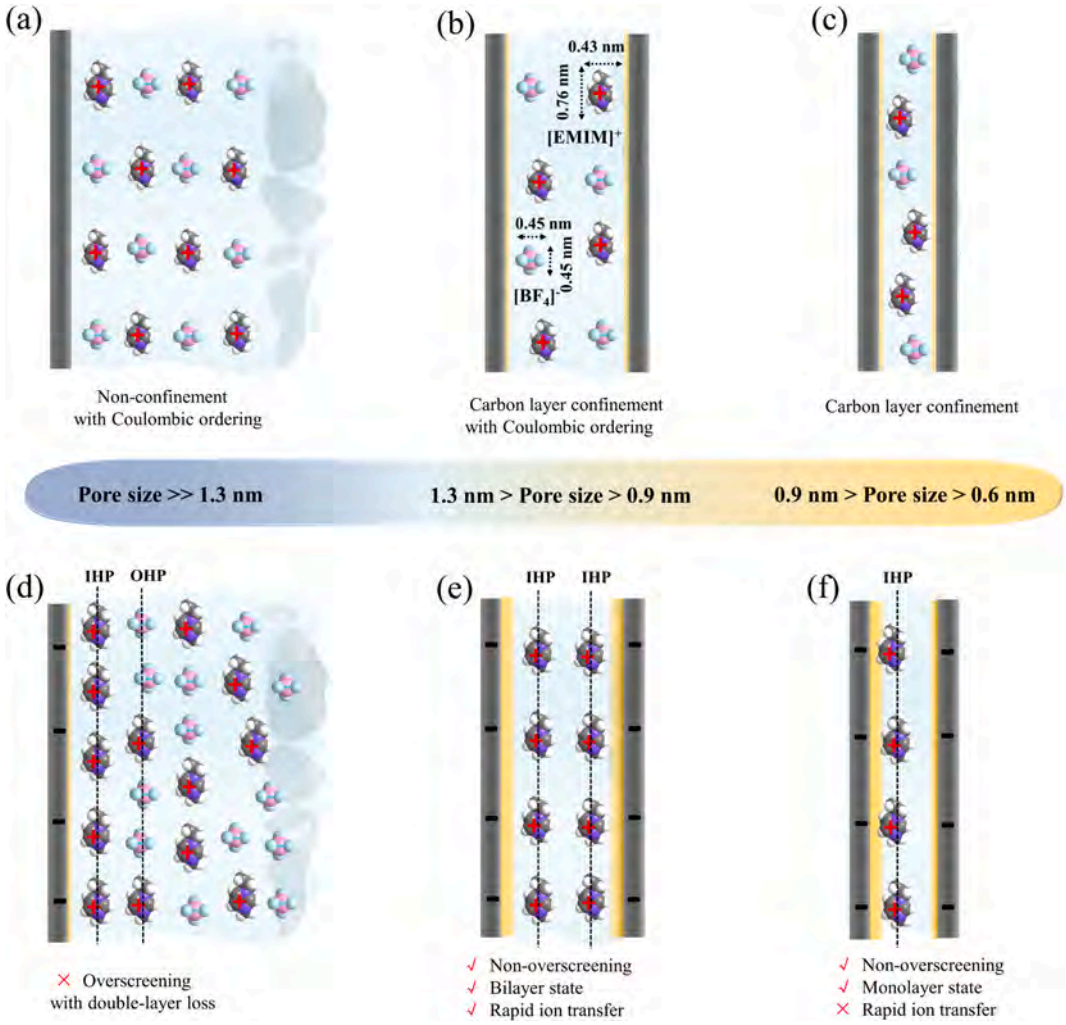

Scheme 1. Adsorption behavior of [EMIM][BF_4] in carbon pores with different size. Standing state: (a) larger than 1.3 nm, (b) between 0.9 and 1.3 nm (bilayer ion pore), (c) between 0.6 and 0.9 nm (monolayer ion pore). (d–f) Corresponding carbon pores surface during negative charging.

2. Results and discussion

As illustrated in Fig. 1a, abundant and large-scale coconut shells were used as the raw materials to synthesize the 3DPFC *via* the molten salt strategy, in which different types of carbon atoms interact with pre-embedded K_2CO_3/Na_2CO_3 to trigger the molecules to form the ultra-thin graphene sheets with an open porous structure and numerous active sites. During the pre-carbonization process, hydrogen atoms are connected to carbon atoms with sp^3 hybridized structures on the surface of graphite microcrystals or to carbon atoms at the edges of graphite microcrystals. These sp^3 hybridized structures interconnect at the edges to bind a large number of graphite microcrystals together and restrict their movement (Fig. 1b). When the temperature reaches the melting point, the solid K_2CO_3/Na_2CO_3 transitions into a liquid molten salt., which allows the graphite microcrystals released by carbon black to disperse within the liquid K_2CO_3/Na_2CO_3 molten salt, thus enabling them to move freely to contact with each other. Within the biocarbon graphite microcrystals, K_2CO_3/Na_2CO_3 primarily facilitates the reaction and consumption of sp^3 cross-linked carbon atoms. Simultaneously, the potassium/sodium metal atoms are produced to act as catalysts for the polymerization of graphite microcrystals, leading to the formation of graphene sheet-like structures [9,19] Additionally, some hydrogen atoms at the edges of these microcrystals may serve as reaction sites, where the charge transfer complex removes the hydrogen atoms, allowing for the formation of new sp^2 hybridized bonds. As these graphite microcrystals combine and gradually grow, a large graphene lattice is eventually formed. Furthermore, since the process occurs in a liquid phase, the graphene layers may draw close and attract each other through van der Waals forces, resulting in the formation of different graphene sheets. Furthermore, the carbon samples prepared by double salt obtain a higher yield of 20 % than that activated by KOH (<15 %) (Fig. S7b) [20]. For details, as shown in the TG-DTG curve of the K_2CO_3/Na_2CO_3 salt heat treatment process in Fig. S2a. The first significant mass loss happens at approximately 190 °C, which can be attributed to water evaporation. The second mass loss peak at 705 °C corresponds to the eutectic melting point of K_2CO_3/Na_2CO_3. Furthermore, it is evident that the mass of the mixture decreases rapidly at 850 °C, likely due to the activation and catalytic effects of the molten salt interacting with biogenic carbon, this will lead to the release of gases such as CO, CO_2, CH_4 and H_2 *etc.* [11,21] When the temperature reaches 1050 °C, the activation of carbon by the molten salt is essentially complete, and the mass change gradually slows until stabilizes by the total weight decreasing approximately 65.5 %. The phase compositions of the activated products synthesized at 900 °C were analyzed using *Ex-situ* XRD (Fig. S2b). The analysis detected potassium and sodium carbonates, potassium and sodium oxides, as well as potassium, sodium and graphite intercalation compounds. These findings indicate that K_2CO_3/Na_2CO_3 not only promotes the graphitization process of carbon but also induces the formation of porous structures. When the reaction temperature exceeds 700 °C, the reaction between K_2CO_3/Na_2CO_3 and biocarbon proceeds as follows [19,22]:

$$K_2CO_3 + C \rightarrow K_2O + 2CO \quad (1)$$

$$K_2CO_3 \rightarrow K_2O + CO_2 \quad (2)$$

$$K_2O + C \rightarrow 2K + CO \quad (3)$$

$$CO_2 + C \rightarrow 2CO \quad (4)$$

$$Na_2CO_3 + C \rightarrow Na_2O + 2CO \quad (5)$$

$$Na_2CO_3 \rightarrow Na_2O + CO_2 \quad (6)$$

$$Na_2O + C \rightarrow 2Na + CO \quad (7)$$

The morphologies of the samples were observed using SEM and TEM. The biomass-derived carbon exhibited an uneven surface with the presence of pores, which facilitated the permeation of salt in catalyzing the growth of graphene sheets as shown in Fig. S3. The surface of 3DPFC-

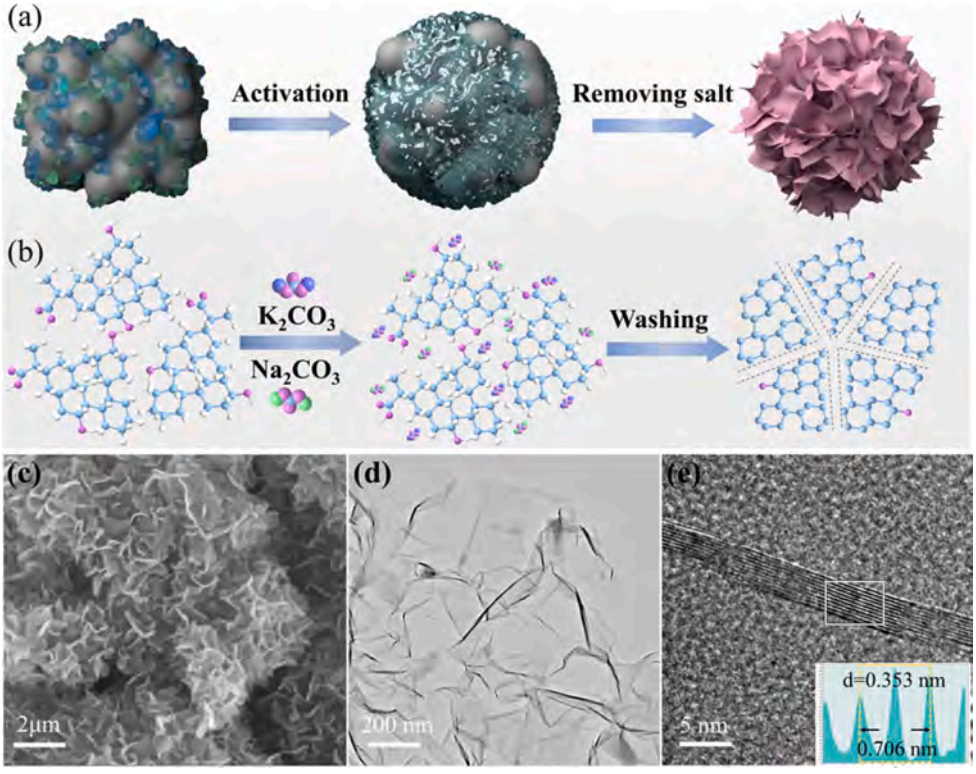

Fig. 1. (a) Schematic illustration of the formation mechanism of activated 3DPFC by K_2CO_3/Na_2CO_3 activation. (b) The aggregation microtopography of K_2CO_3/Na_2CO_3 activation changes. (c) SEM images of, 3DPFC-900. (d) TEM images of 3DPFC-900. (e) High-resolution TEM images of 3DPFC-900.

850 reveals numerous tiny, upright nanosheets (Fig. S4a), while 3DPFC-900 shows intertwined, aligned graphene nanosheets that interconnect to form a 3D flower-like structure with abundant open pores of varying sizes (Fig. 1c). These open pores form spaces between neighboring layers, with the curled edges of the nanosheets preventing agglomeration. This interconnected, porous framework serves as an ion buffer reservoir during electrochemical testing and facilitates electrolyte ion diffusion into the internal micropores, especially at higher charging rates. However, when the temperature increased to 950 °C, the nanosheets expanded significantly, forming a three-dimensional interconnected macro-porous network, likely as a result of salt volatilization at high temperatures. (Fig. S4d). In contrast, the commercial YP-50F shows obvious wrinkles and uneven pores on the surface (Fig. S5a–b). The TEM images (Figs. 1d and S4b–c) also reveal inherent wrinkles or ripples in the nanosheets, which is similar to previous reports for graphene oxide [23,24]. These wrinkles can effectively prevent the tight stacking of nanosheets when they are packaged or compressed into electrode structures. Furthermore, the lattice fringe distances are measured to be 0.351 nm (3DPFC-850), 0.353 nm (3DPFC-900), and 0.360 nm (3DPFC-950) respectively (Figs. 1e and S4c–f). These distances are slightly larger than the ideal structure of graphite (0.34 nm) and typical functionalized graphene (>0.34 nm) due to doping of heteroatoms such as nitrogen (N), oxygen (O), and phosphorus (P) [25]. To further explore the phase structure and pore size distribution of samples, FTIR, XPS, Raman, and BET were performed. Fig. 2a displays the XRD patterns of the carbon lattices before and after the salt activation. The biocarbon shows two broad diffraction peaks at $2\theta = 23.7^{\circ}$ and 43.9°, corresponding to the (002) and (100) planes, respectively, which is indicative of the typical microcrystalline structure of amorphous carbon [26]. In contrast, the 3DPFC display a significant (002) diffraction peak that slightly shifts to 26.1°, indicating the presence of graphene or graphene-like materials and revealing a high degree of graphitization of 3DPFC induced by the K_2CO_3/Na_2CO_3 salt activation. Raman spectra (Fig. 2b) show characteristic peaks at 1353 cm^{-1} (D-band), 1580 cm^{-1} (G-band), and 2675 cm^{-1} (2D-band), respectively [27]. The G-band is attributed to the in-plane vibration mode of sp^2 carbon, indicating the degree of graphitization, and the D-band corresponds to the breathing mode of sp^3 carbon atoms, indicating structural disorders and defects, the intensity ratio of the D and G band (I_D/I_G) is used to evaluate the level of graphitization. Compared to I_D/I_G of 0.8361 for biocarbon, which represents the existence of many defects of sp^3 carbon atoms in carbon materials with high disorder levels, the 3DPFC show a lower I_D/I_G, indicating an excellent graphene structure.

Given the 2D band represents the second-order zone boundary phonon resonance, which is related to the number of layers in the graphene [28], the 3DPFC show a sharp and strong second-order 2D peak at 2675 cm^{-1} and the low-intensity ratios between 2D and G bands (I_{2D}/I_G = 0.4252) indicates the domination of fewer layers of graphene structure and graphene-like sheets in 3DPFC. These findings align with the HRTEM observations. Following, the FTIR spectra show that the

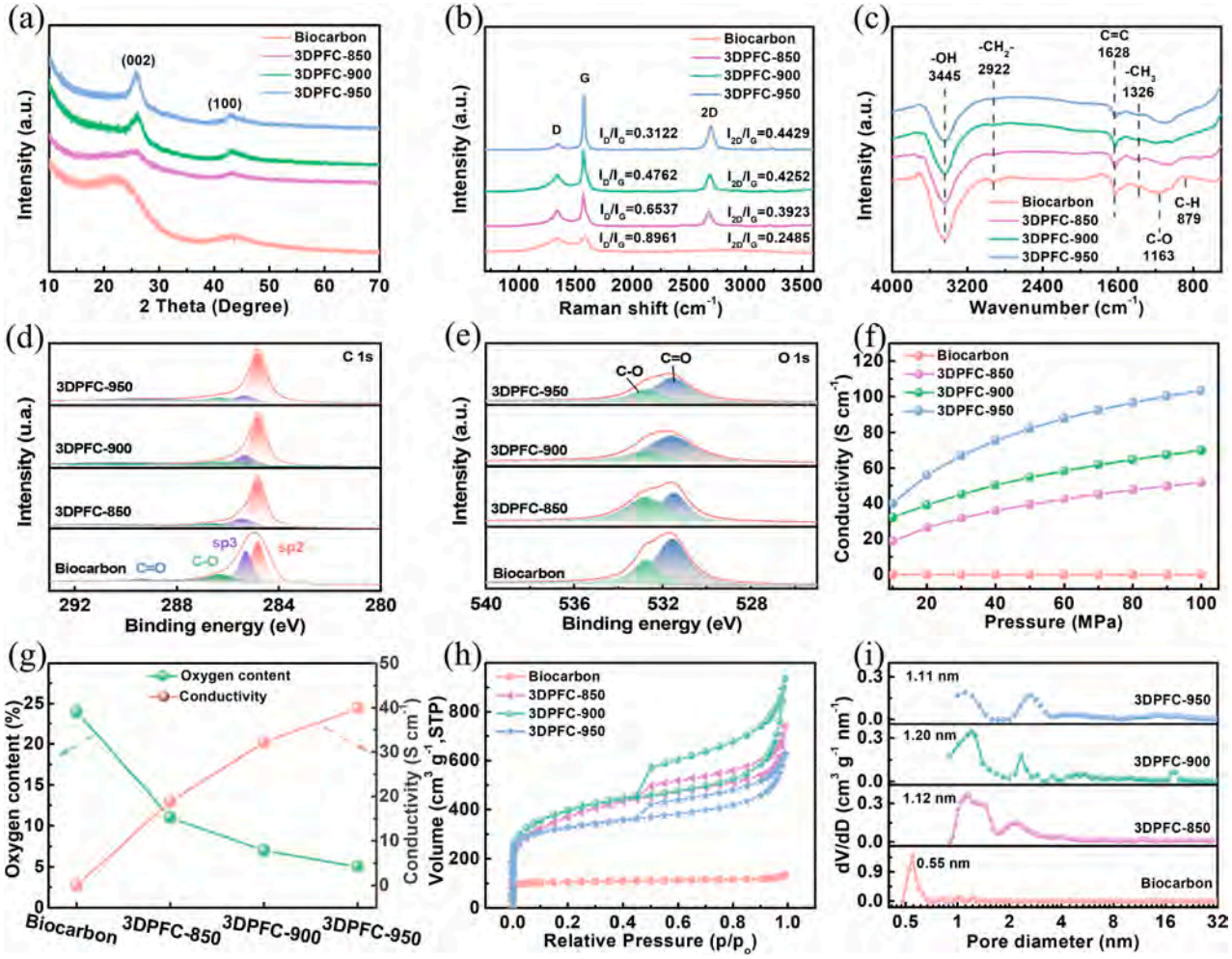

Fig. 2. Physical characterization of samples. (a) X-ray diffractometer (XRD) patterns. (b) Raman spectra. (c) Fourier transform infrared spectroscopy (FTIR) spectra. (d) Fitting curve of C 1s. (e) Fitting curve of O 1s. (f) Comparison of conductivity of sample and YP-50F in different pressures. (g) The relationship between electrical conductivity and oxygen content. (h) N_2 adsorption/desorption isotherms. (i) Pore size distribution by DFT method.

carbonization process gradually occurs through the steady transition from sp^3 C—X (X = C, O, H) bond to the aromatic sp^2 C═C bond. In Fig. 2c, the biocarbon exhibits peaks associated with −O—H stretching (3345 cm^{-1}), –CH_2– expansion vibration (2922 cm^{-1}), the symmetrical–CH_3 (1326 cm^{-1}), and the C—O stretching (1163 cm^{-1}) [29,30]. Besides, the peak at around 1620 cm^{-1} (C═C stretching) and 879 cm^{-1} (C—H stretching) can be attributed to sp^2-bonded benzene rings [31,32]. Obviously, after salt activation, the FTIR curves of 3DPFC become smoother, and the intensities of the C—O and C—H groups decrease significantly, this phenomenon indicates a reduction in oxygen-containing functional groups consume and a strong absorption of sp^2-bonded carbon in the infrared region [33]. XPS analysis (Fig. 2d) further confirms the presence of carbon and oxygen and no impurities remained (Fig. S6a and Table S1). Due to the fewer impurities in the raw materials of coconut shells, the ash content of porous carbon is <0.2 %, which successfully solves the problem of high ash content of porous carbon derived from biomass (Fig. S7a). In detail, the C 1s spectra of the biocarbon and 3DPFC were deconvoluted into two peaks (284.8 and 285.3 eV) corresponding to the sp^2 C atoms and sp^3 C atoms, respectively [34,35]. Additional peaks at 286.3 and 289.5 eV in the C 1s spectra suggest the presence of oxygen functionalities such as C—O and C═O groups (Fig. 2d) [36]. The content of sp^2 C atoms increased from 45.74 to 70.13 at.% after the salt activation, while the contents of sp^3 C, C—O and C═O decreased significantly, which confirms the enhancement of graphitization and reduction of oxygen-containing groups (Table S1). In Fig. 2e, the O 1s spectra show two fitting peaks at 531.5 eV (C═O) and 532.8 eV (C—O), further demonstrating that salt activation can obviously increase the sp^2 C and tailor the structure of graphitization. The XPS characterization results further demonstrated that with the increase of temperature, the oxygen signal decreases in 3DPFC, which is attributed to the loss of high-temperature activated oxygen elements [21]. As the oxygen content decreases, the conductivity of the sample increases due to the breakage of weak carbon-oxygen bonds and the formation of highly conductive sp^2 hybridized bonds (Fig. 2f–g). The 3DPFC-900 exhibit high conductivity (32.15 S cm^{-1}) at 10 MPa, far exceeding that of other three-dimensional graphene prepared by other methods (2–10 S cm^{-1}) and even commercial high-performance capacitors used YP-50F (3.6 S cm^{-1}) (Figs. 2f and S6b) [37–39]. In addition, 3DPFC-900 also exhibit excellent conductivity and high pressure real density, inheriting the highly dense characteristics of biocarbon (Fig. S6c). In Fig. S6d, the relatively low metal content of 3DPFC-900 is beneficial to the electrical conductivity.

The pore structures and specific surface area of the samples were evaluated by N_2 adsorption-desorption measurements as shown in Fig. 2h. The isotherms curve of biocarbon exhibits type-I isotherm with a sharp adsorption knee at relatively low pressures ($P/P_0 < 0.01$) and a well-developed plateau at higher pressures, which is typical for microporous materials, thus indicating predominantly microporous characteristics. With the addition of K_2CO_3 and Na_2CO_3 salt, the isotherms of the samples change to a combination of type I and IV isotherms with strong N_2 adsorption at a low relative pressure ($P/P_0 < 0.01$), and an obvious H_4 hysteresis loop at a relative pressure of $0.4 < P/P_0 < 1$, indicating an interconnected pore system consisting of both micropores and mesopores [40]. The pore size distribution (Fig. 2i) shows that biocarbon predominantly features micropores with negligible pores larger than 3 nm observed by the DFT method. In contrast, the 3DPFC exhibit a well-developed porous structure including ultra-micropores (<2 nm), small mesopores (2–4 nm), and distinct meso- to macropores (2–70 nm), which are consistent with SEM/TEM analyses. The abundant micropores provide abundant adsorption sites, resulting in a higher specific capacitance, while the mesopores serve as electrolyte transport channels and buffer channels for electrolytes. For comparison, the YP-50F has a high specific surface area of 1760 m^2 g^{-1}, but its pore size distribution is centrally distributed in the micropore region (<2 nm) (Fig. S7c–d). Furthermore, more detailed information on SSA and porosity are summarized in Table S2. The SSA of 3DPFC-850, 3DPFC-900 and 3DPFC-950 were found to be 1469, 1701 and 1224 m^2 g^{-1}, respectively, with larger total pore volumes of 0.841 and 0.932 and 0.794 cm^3 g^{-1}, compared to the biocarbon (401 m^2 g^{-1}, 0.208 cm^3 g^{-1}). During the activation process, carbonates not only react with biochar to form interconnected pore structures but also generate potassium and sodium metals to further catalyze the growth of graphene-like sheets. These results indicate the enhanced activation and degree of graphitization by a mixture K_2CO_3 and Na_2CO_3 salt (Fig. S7e–f).

To further explore the possibility of the designed materials for the commercial application, the organic electrolyte has been applied to assembling organic electrolyte-based supercapacitor. The contact angle test further showed that the contact angle of 3DPFC-900 in [EMIM][BF_4]/PC electrolyte (15.1°) was significantly smaller than that of YP-50F (75.3°) (Fig. S13). Such good wettability of 3DPFC-900 is beneficial from flower-like carbon skeleton nanosheets and open microporous-mesoporous-macroporous pores. To further compare the electrochemical performance of 3DPFC-900 (denoted as 3DPFC-900//3DPFC-900) and YP-50F (denoted as YP-50F//YP-50F), the symmetrical supercapacitors were assembled using [EMIM][BF_4]/PC electrolyte with a relatively high voltage window of 3.0 V. Obviously, 3DPFC-900 exhibited an ideal rectangular shape without substantial distortions for indicating an ideal electric double layer (EDL) capacitance (Fig. 3a–b). It is worth noting that the CV curve of the YP-50F sample exhibits a very sharp peak from 2.0 V–2.5 V (Figs. 3a and S14a). At a current density of 1 A g^{-1}, the YP-50F charges only up to 2.525 V, suggesting that its curved pores or high oxygen-containing functional groups hinder the rapid ion transfer at high voltages or lead to gas production that disrupts proper operation (Figs. 3c and S14a–e). In contrast, GCD profiles of 3DPFC-900 display high symmetry at the current densities of 1 A g^{-1}, indicating good kinetic reversibility and excellent coulombic efficiency (Figs. 3c–d and S14f). The reduced oxygen content of the sample electrodes facilitates high voltages in organic electrolytes and also prevents oxidation of the electrodes during charging and discharging, thus leading to the suppression of serious problems such as gas escape (CO and CO_2, *etc.*) and polarization [41,42]. According to Fig. 3e, 3DPFC-900 exhibited higher ion affinity (CEDL = 70.51) than YP-50F (CEDL = 36.64), thus 3DPFC-900 possessed the higher theoretical electrochemical active surface area. The rate performance of 3DPFC-900 can reflect their efficiency during the charge and discharge process. Fig. 3f shows that the specific capacitance of 3DPFC-900 capacitors can be as high as 175 and 112 F g^{-1} at 0.5 and 30 A g^{-1}, respectively, which are higher than that of the YP-50F capacitors (81.7 F g^{-1} at 1 A g^{-1} and 24 F g^{-1} at 30 A g^{-1}). Even at the high current density of 50 A g^{-1}, the 3DPFC-900-based supercapacitor delivers a high specific capacitance of 106 F g^{-1}. The Nyquist diagram of 3DPFC-900 and YP-50F (Fig. 3g). The equivalent series resistances of 3DPFC-900 are 10.1 Ω, which is smaller than that of YP-50F (20.6 Ω). In addition, the angle between the linear part of the low-frequency region and the Y-axis of 3DPFC-900 is significantly smaller and more perpendicular than that of YP-50F. The smaller semicircle diameter in the high-frequency region indicates a faster ion transport rate and lower charge transfer resistance. Furthermore, the 3DPFC-900-based capacitors possess an ultrahigh energy density of 109 Wh kg^{-1} and high-power density of 71 kW kg^{-1}, which is higher than the commercial activated carbon (YP-50F) capacitors with an energy density of 35.4 Wh kg^{-1} and a power density of 37.5 kW kg^{-1} (Fig. 3h). Such excellent performance of 3DPFC-900 is also outperforming other carbon-based supercapacitors (Fig. 3h and Table S4) [43,44]. Finally, when assembled into a soft-pack capacitor device, the 3DPFC-900 based capacitors can also show a satisfactory power density that can light up the diode (LED) for 30 min (Figs. 3h and S13). Remarkably, even after 40,000 charge/discharge cycles at an ultrahigh current density of 20 A g^{-1}, the 3DPFC-900 electrode exhibited excellent capacity retention (90.3 %) along with a near-perfect Coulombic efficiency (99.98 %), highlighting its superior cycling durability and electrochemical reversibility for practical applications (Fig. 3i).

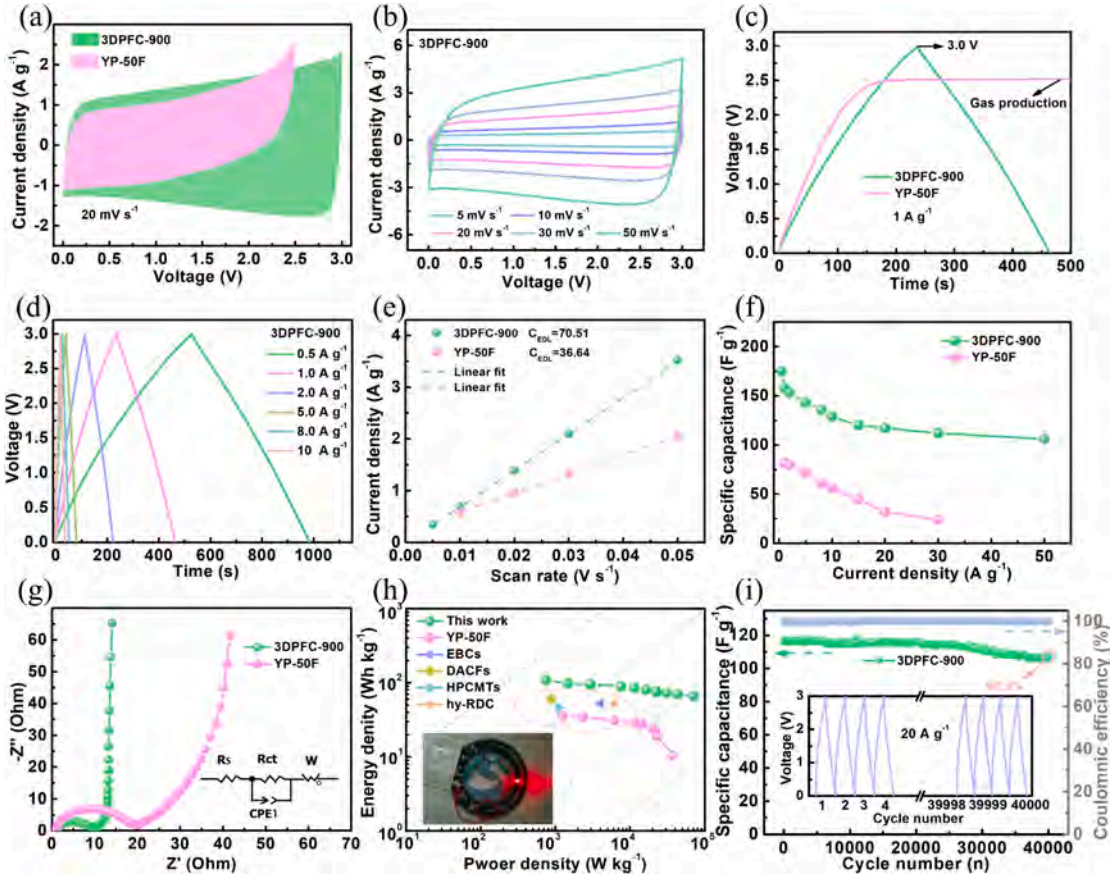

Fig. 3. The electrochemical properties of 3DPFC-900 and YP-50F based supercapacitors in [EMIM][BF_4]/PC electrolyte. (a) CV curves of 3DPFC-900 and YP-50F, (b) CV curves of 3DPFC-900. (c) GCD curves of 3DPFC-900 and YP-50F at 1 A g^{-1}. (d) GCD curves of 3DPFC-900. (e) The *I-ν* plot of electrode materials at 1.0 V. (f) The mass-specific capacitance of 3DPFC-900 and YP-50F capacitors at the different current densities. (g) Nyquist plots, h) Ragone plots of 3DPFC-900 and YP-50F capacitors. (i) Cycling stability of 3DPFC-900 capacitor at 20 A g^{-1}.

To better understand the electrochemical behavior of the 3DPFC-900 electrodes, *In-situ* FT-IR, *In-situ* Raman, and *Ex-situ* XPS characterizations are employed. As shown in *In-situ* Raman spectra, the D-peak area of the electrode decreases with increasing potential, which is mainly due to the vibration effect of sp^2 C atom (Figs. 4a–c and S16). The area of D-peak decreased with the increase in charging time, indicating that the interaction between electrolyte ions and the defect site on the electrode surface inhibited the A_{1g} mode in D-band (Fig. 4c). Interestingly, with charging progresses, peak D shifts to the left and gradually becomes weak or disappears, implying that electrolyte ions are adsorbed at the defect (Fig. 4b). During the charging process, the ratio of area D peak to area G peak (S_D/S_G) value gradually decreases, which is attributed to the continuous adsorption of electrolyte ions in the disordered structure of 3DPFC-900 such as defects and edge active sites, thus resulting in a decrease in the degree of defects. During the subsequent discharging process, the S_D/S_G value gradually returned to its initial level, illustrating the good structural stability of 3DPFC-900 (Fig. S16a). In contrast, the area of the G peak remains unchanged during the discharge process, suggesting that the interaction between electrolyte ions and electrodes is only physical adsorption. *In-situ* FT-IR was applied to analyze the kinetic behavior of 3DPFC-900 and electrolyte ions (Fig. 4d–e). During the charging process, given the adsorption of electrolyte ions on the carbon edge surface will affect the C=C stretching vibration, the infrared absorption intensity of the electrode is gradually reduced. When voltage further increases, the infrared absorption intensity of the electrode gradually decreases, which indicates that electrolyte ions enter the pores and form double-layer adsorption in the inner Helmholtz layer (Fig. 4c). In addition, during the charging/discharging process of the electrode, there is a process of ion diffusion and adsorption (dissociation and diffusion). During the initial charging process, the ion diffusion process occurs on the electrode surface, that is, the anions and cations migrate to the positive and negative electrodes respectively. At this time, the B—F peak (1054 cm^{-1}) on the negative surface is weak and C—N (1258 cm^{-1}) is strong (diffusion process). Therefore, A gradual enhancement of the C—N has been detected with the charging process, which means that the $[EMIM]^+$ is continuously adsorbed to the electrode surface (Fig. 4d) [45,46]. When the voltage rises above 2.5 V, the characteristic peak of C—N weakens, while that of B—F intensifies. This phenomenon indicates that the $[BF_4]^-$, which were initially randomly adsorbed in the carbon pores, undergo desorption and efflux from the pores. Concurrently, $[EMIM]^+$ ions ingress into the carbon pores and occupy the active sites vacated by the desorption of $[BF_4]^-$, thereby facilitating ion exchange [3,47]. During the discharging process, the vibrational signals of the C—N bonds also gradually weakened, indicating that the cations slowly released from the electrode surface. In addition, during the discharging, the efflux of $[EMIM]^+$ and the inward flow of $[BF_4]^-$, forming an ion exchange mechanism, may not be detected because of the fast $[BF_4]^-$ influx, and only $[EMIM]^+$ is detected (Fig. 4e) [16].

The *Ex-situ* XPS measurements were performed on 3DPFC-900 electrodes (negative) to further investigate the electrolyte ions. From the XPS spectra of N 1s (Fig. 4f), it can be seen that a diffraction peak belonging to pyridine-N appears at 0 V, which may come from the sample itself. With the voltage charging to 1.3 V, one more pyrrolic-N appears on the spectra due to the presence of adsorbed $[EMIM]^+$, and the intensity of the peak becomes stronger when charged to 3 V,

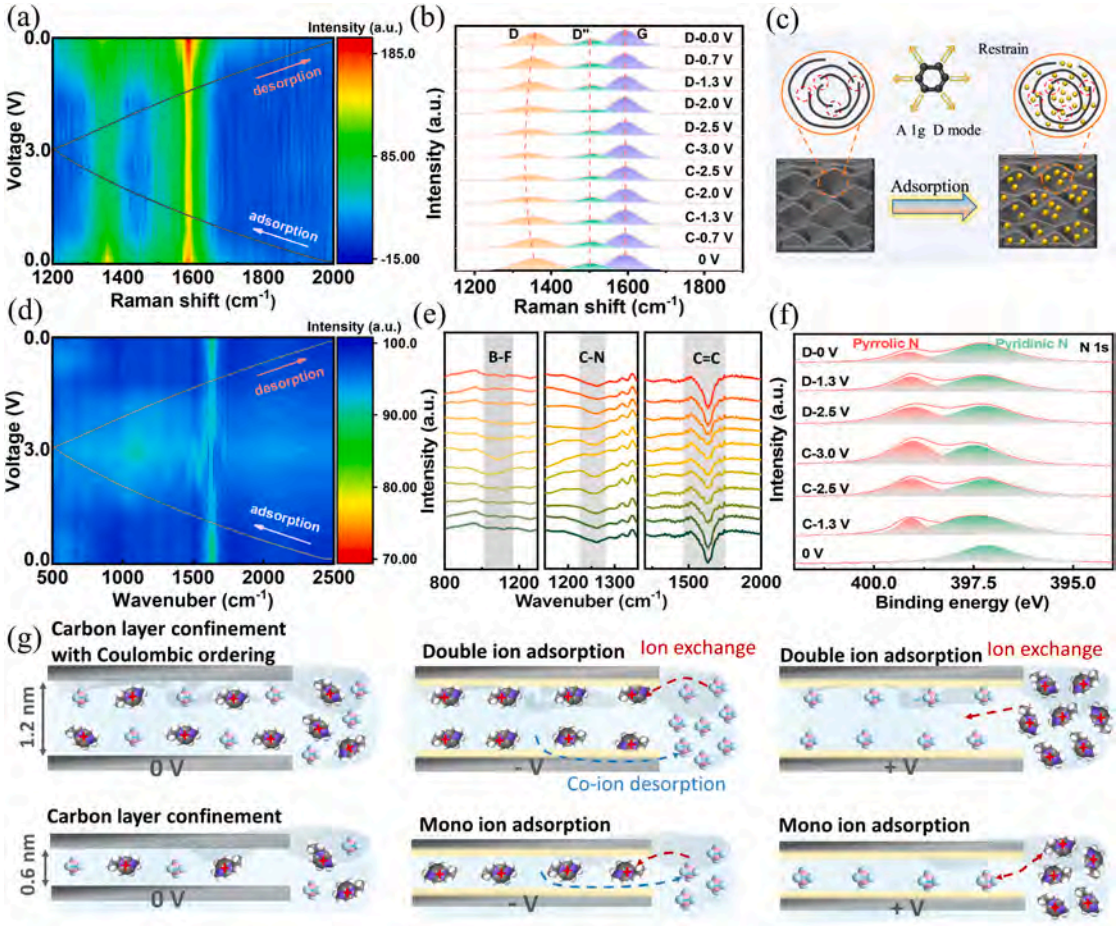

Fig. 4. Electrochemical mechanism of ion transport for 3DPFC-900 based supercapacitor. (a, b) *In situ* Raman spectroscopy at different charging states. (c) Schematic illustration of active ion storage in defect carbon. (d, e) *In situ* FTIR curve of the negative electrode at different charging states. (f) *Ex situ* XPS spectra of N 1s for negative electrode at different voltages. (g) Schematic illustration of the charge-storage mechanism in bilayer confinement and monolayer confinement pores in the unbiased, negatively, and positively biased states.

suggesting that more $[EMIM]^+$ ions have been adsorbed. When discharging, the peak intensity gradually diminishes, indicating that $[EMIM]^+$ ions are gradually desorbed (Fig. S16b). In addition, the trend of the XPS curve of B 1s was opposite to that of pyrrolic-N, with a smaller area of the peak during charging and an increase in the area of the peak during discharging, suggesting that $[BF_4]^-$ was desorbed and adsorbed (Fig. S16c–d) [48,49].

Based on the above discussion, the charge storage mechanism in the ionophilic 3DPFC-900 has been summarized in Fig. 4g. In bilayer confinement pores, ions adopt a Coulomb-ordered arrangement, while in monolayer confinement pores, they exist in an ion-pair state [17]. Both configurations support ion exchange and co-ion desorption during charging. Under negative bias in bilayer confinement, a double-layer $[EMIM]^+$ arrangement forms, whereas under positive bias, a double-layer $[BF_4]^-$ arrangement appears. In monolayer confinement, $[EMIM]^+$ and $[BF_4]^-$ ions align as single layers under negative and positive biases, respectively. Compared to monolayer adsorption, the vertical alignment of $[EMIM]^+$ in negatively charged bilayers may provide the optimal configuration for achieving high storage density and rapid ion dynamics.

Taking into account the larger size of $[EMIM]^+$ (0.76 nm) compared to $[BF_4]^-$ (0.45 nm), this study explores the adsorption models of $[EMIM]^+$ and its corresponding planar average charge density difference in various sized carbon pores *via* DFT calculations to further elucidate the ion adsorption mechanism. For carbon pores with a size of 0.6 nm, the $[EMIM]^+$ exhibit an approximately symmetrical structure and are located at the center axis position of the carbon pore (Fig. S17a). When the pore size is increased to 0.7 nm, the $[EMIM]^+$ structure rotates, but they still remain close to the center axis position (Fig. S17b). As the pore size further increases, the $[EMIM]^+$ structure tends to stabilize and parallelly adsorb on the left carbon wall (Fig. S17c–h). Fig. 5a presents the charge density difference per unit volume (Δp) of a single $[EMIM]^+$ adsorbed onto the left carbon wall (ΔpL) and the right carbon wall (ΔpR) in carbon pores with different sizes. When the carbon pore size is within the range between 0.6 and 0.7 nm, ΔpL and ΔpR are proximate, which suggests that the interaction between $[EMIM]^+$ and the two carbon walls on either side are approaching equilibrium (Figs. 5a and S18a). To this point, the migration and adsorption of $[EMIM]^+$ are influenced by the two carbon walls equally. When the pore size increases from 0.7 nm to 1.0 nm, ΔpL rises from 0.3×10^{-3} to 0.35×10^{-3} e/Å^3, while ΔpR drops rapidly to 0.15×10^{-3} e/Å^3, demonstrating that as the pore size enlarges, the interaction between $[EMIM]^+$ and the left carbon wall gradually increases, while the interaction with the right carbon wall weakens (Figs. 5c and S18b–c). When the pore size of carbon increases beyond 1.0 nm, the growth rate of ΔpL decelerated conspicuously, indicating that $[EMIM]^+$ mainly interacts with the left carbon wall in larger-sized pores (Figs. 5d–e and S18d). Previous reports have primarily focused on ion adsorption and storage mechanisms with pore sizes <1.0 nm, while a comprehensive understanding of these mechanisms for pore sizes ranging from 1.0 to 1.3 nm remains insufficient. Therefore, our findings further expand the ion adsorption models and storage mechanisms of the two $[EMIM]^+$ within the pore size range of 1.0 to 1.3 nm (Fig. S19a–d). When the size of carbon pores is >1.0 nm, monotonic adsorption of double-layer $[EMIM]^+$ can be attained, which

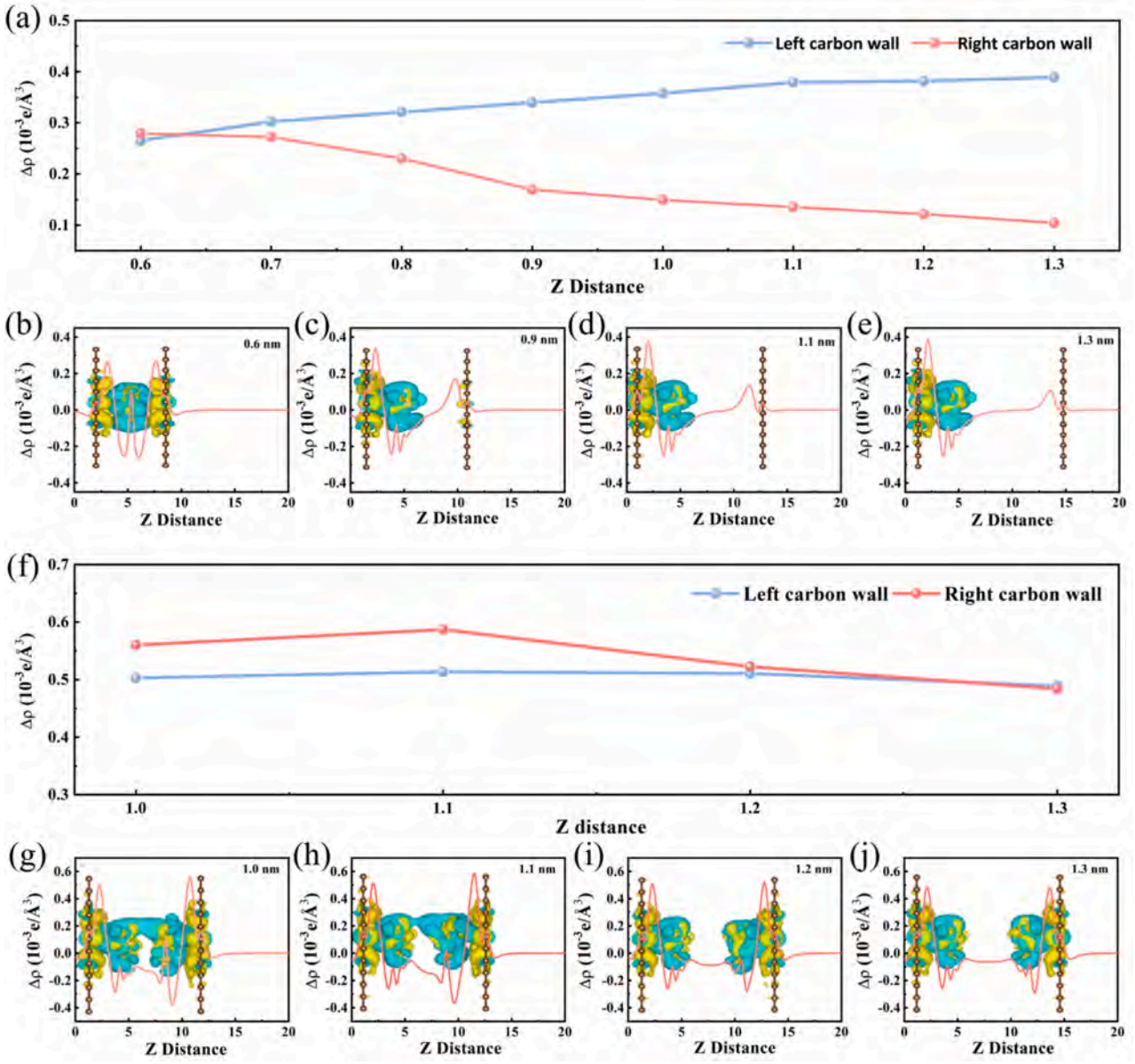

Fig. 5. Theoretical understanding of $[EMIM]^+$ adsorption mechanism on various carbon pore sizes. (a) Charge density difference per unit volume of single $[EMIM]^+$ at the left (blue dotted line) and right (red dotted line) carbon walls in various carbon pore sizes. The planar average charge density difference of a $[EMIM]^+$ adsorbed in carbon pores with a pore size of (b) 0.6 nm, (c) 0.9 nm (d) 1.1 nm, and (e) 1.3 nm. (f) Charge density difference per unit volume of two $[EMIM]^+$ at the left (blue dotted line) and right (red dotted line) carbon walls in various carbon pore sizes. The planar average charge density difference of two $[EMIM]^+$ adsorbed in carbon pores with a pore size of (g) 1.0 nm, (h) 1.1 nm, (i) 1.2 nm, and (j) 1.3 nm.

is different from traditional $[EMIM]^+$ monolayer adsorption. As illustrated in Fig. 5f–j, the charge transfer between $[EMIM]^+$ and carbon walls is greater than that between $[EMIM]^+$. When the carbon pores size increases from 1.0 to 1.2 nm, the differential charge density difference per unit volume between the two carbon walls and the $[EMIM]^+$ adsorbed on their surfaces, as well as the charge transfer between the two $[EMIM]^+$, tends to zero. The foregoing results indicate that a carbon pore size of 1.2 nm not only accelerates ion diffusion and exchange but also enables double-layer monotonic ion adsorption, significantly boosting the power and energy density of the 3DPFC-900. This aligns well with the results from electrochemical performance tests.

3. Conclusions

In summary, we have successfully prepared 3DPFC through a simple double carbonate activation process using bio-waste coconut shells as a precursor, enabling continuous large-scale production. During the thermal reaction, catalytic activation and pore formation by intermediate products allow molten carbonate to fully contact pre-carbonized biomass. This process promotes the free diffusion, polymerization, and growth of graphite microcrystals, resulting in 3DPFC with a large specific surface area, interconnected microporous-mesoporous structure, and low oxygen content. The high specific surface area increases active sites and improves ion adsorption capacity, while carbonates catalyze the conversion from sp^3 to sp^2 carbon, reducing oxygen content and enhancing both electrical conductivity and oxidation resistance at high voltages. The hierarchical pore system not only facilitates ion transport and diffusion by providing interconnected channels but also enables dual adsorption of anions and cations, further boosting ion storage. Furthermore, we show that ions in carbon pores with a 1.2 nm diameter achieve double-layer parallel adsorption without overshielding, maximizing ion storage utilization and diffusion dynamics, which leads to the

proposal of a "dual-layer ionic monotonic adsorption mechanism". As anticipated, the 3DPFC-based supercapacitors deliver an ultrahigh energy density of 109 Wh kg^{-1} and a power density of 71,000 W kg^{-1} in [EMIM][BF_4]/PC electrolyte. This work offers a novel pathway for designing and manufacturing low-cost, high-capacity, high-voltage-resistant carbon materials for supercapacitors with high power and energy densities.

CRediT authorship contribution statement

Gaojie Li: Writing – review & editing, Writing – original draft, Validation, Methodology, Investigation, Formal analysis, Data curation. **Xinbo Guo:** Validation, Project administration, Data curation, Conceptualization. **Yu Liu:** Writing – review & editing, Visualization, Validation, Supervision, Project administration. **Jianguo Sun:** Validation, Software, Conceptualization. **Hang Yang:** Validation, Software. **Yang Zheng:** Visualization, Validation. **Xuming Zhang:** Validation, Supervision. **Paul K. Chu:** Validation, Supervision. **Guanjie He:** Writing – review & editing, Validation, Supervision. **Biao Gao:** Writing – review & editing.

Declaration of competing interest

The authors declare that they have no known competing financial interests or personal relationships that could have appeared to influence the work reported in this paper.

Acknowledgments

This work was financially supported by the Hubei Provincial Science and Technology Research Project (2024BAA012), the China Postdoctoral Science Foundation under, Grant, Number 2024M752495, the Postdoctoral Fellowship Program of CPSF under Grant Number GZB20230552, the National Key Research and Development Program of China (2022VFB2404800) and the Knowledge Innovation Project of Wuhan City (2022010801010303). The authors are grateful for the facility support provided by the Analytical and Testing Center of WUST.

Appendix A. Supplementary data

Supplementary data to this article can be found online at https://doi.org/10.1016/j.cej.2025.165799.

Data availability

Data will be made available on request.

References

[1] X. Liu, D. Lyu, C. Merlet, M. Leesmith, X. Hua, Z. Xu, C. Grey, A. Forse, Structural disorder determines capacitance in nanoporous carbons, Science 384 (2023) 321–325, https://doi.org/10.26434/chemrxiv-2023-bd24m.
[2] P. Simon, Y. Gogotsi, Perspectives for electrochemical capacitors and related devices, Nat. Mater. 19 (2020) 1151–1163, https://doi.org/10.1038/s41563-020-0747-z.
[3] Z. Li, S. Gadipelli, H. Li, C.A. Howard, D.J.L. Brett, P.R. Shearing, Z. Guo, I. P. Parkin, F. Li, Tuning the interlayer spacing of graphene laminate films for efficient pore utilization towards compact capacitive energy storage, Nat. Energy 5 (2020) 160–168, https://doi.org/10.1038/s41560-020-0560-6.
[4] G. Nagaraju, S.C. Sekhar, B. Ramulu, S.K. Hussain, D. Narsimulu, J.S. Yu, Ternary mof-based redox active sites enabled 3D-on-2D nanoarchitectured battery-type electrodes for high-energy-density supercapatteries, Nano-Micro Lett. 13 (2020), https://doi.org/10.1007/s40820-020-00528-9.
[5] B. Jia, B. Zhang, Z. Cai, X. Yang, L. Li, L. Guo, Construction of amorphous/crystalline heterointerfaces for enhanced electrochemical processes, eScience 3 (2023) 100112, https://doi.org/10.1016/j.esci.2023.100112.
[6] J. Du, Q. Han, Y. Chen, M. Peng, L. Xie, A. Chen, Micro/meso-porous double-shell hollow carbon spheres through spatially confined pyrolysis for supercapacitors and zinc-ion capacitor, Angew. Chem. Int. Ed. 63 (2024) e202411066, https://doi.org/10.1002/anie.202411066.
[7] I. Hussain, C. Lamiel, S. Sahoo, M.S. Javed, M. Ahmad, X. Chen, S. Gu, N. Qin, M. A. Assiri, K. Zhang, Animal- and human-inspired nanostructures as supercapacitor electrode materials: a review, Nano-Micro Lett. 14 (2022), https://doi.org/10.1007/s40820-022-00944-z.
[8] X. Li, C. Cai, P. Hu, B. Zhang, P. Wu, H. Fan, Z. Chen, L. Zhou, L. Mai, H.J. Fan, Gradient pores enhance charge storage density of carbonaceous cathodes for zn-ion capacitor, Adv. Mater. 36 (2024), https://doi.org/10.1002/adma.202400184.
[9] Q. Gou, S. Zhao, J. Wang, M. Li, J. Xue, Recent advances on boosting the cell voltage of aqueous supercapacitors, Nano-Micro Lett. 12 (2020), https://doi.org/10.1007/s40820-020-00430-4.
[10] H. Wu, W. Yuan, X. Yuan, L. Cheng, Atmosphere-free pyrolysis of harakeke fiber: a new chamber-induced activation methodology for porous carbon electrodes in supercapacitors, Energy Storage Mater. 50 (2022) 514–524, https://doi.org/10.1016/j.ensm.2022.05.046.
[11] L. Sun, K. Zhuo, Y. Chen, Q. Du, S. Zhang, J. Wang, Ionic liquid-based redox active electrolytes for supercapacitors, Adv. Funct. Mater. 32 (2022), https://doi.org/10.1002/adfm.202203611.
[12] X. Li, C. Cai, L. Zhou, L. Mai, H. Fan, Unraveling the capacitive behaviors in nanoconfined ionophilic carbon pores, Adv. Mater. 36 (2024) 2404393, https://doi.org/10.1002/adma.202404393.
[13] J. wu, M. Xia, X. Zhang, Y. Chen, F. Sun, X. Wang, H. Yang, H. Chen, Hierarchical porous carbon derived from wood tar using crab as the template: performance on supercapacitor, J. Power Sources 455 (2020) 227982, https://doi.org/10.1016/j.jpowsour.2020.227982.
[14] Z. Liu, C. Duan, S. Dou, Q. Yuan, J. Xu, W. Liu, Y. Chen, Ultrafast porous carbon activation promises high-energy density supercapacitors, Small 18 (2022) 2200954, https://doi.org/10.1002/smll.202200954.
[15] S. Fleischmann, Y. Zhang, X. Wang, P.T. Cummings, J. Wu, P. Simon, Y. Gogotsi, V. Presser, V. Augustyn, Continuous transition from double-layer to faradaic charge storage in confined electrolytes, Nat. Energy 7 (2022) 222–228, https://doi.org/10.1038/s41560-022-00993-z.
[16] R. Futamura, T. Iiyama, Y. Takasaki, Y. Gogotsi, M.J. Biggs, M. Salanne, J. Ségalini, P. Simon, K. Kaneko, Partial breaking of the coulombic ordering of ionic liquids confined in carbon nanopores, Nat. Mater. 16 (2017) 1225–1232, https://doi.org/10.1038/nmat4974.
[17] M. Antonietti, X. Chen, R. Yan, M. Oschatz, Storing electricity as chemical energy: beyond traditional electrochemistry and double-layer compression, Energy Environ. Sci. 11 (2018) 3069–3074, https://doi.org/10.1039/c8ee01723a.
[18] H. Shao, Y.C. Wu, Z. Lin, P.L. Taberna, P. Simon, Nanoporous carbon for electrochemical capacitive energy storage, Chem. Soc. Rev. 49 (2020) 3005–3039, https://doi.org/10.1039/d0cs00059k.
[19] X. Du, Z. Lin, Y. Zhang, P. Li, Microstructural tailoring of porous few-layer graphene-like biochar from kitchen waste hydrolysis residue in molten carbonate medium: structural evolution and conductive additive-free supercapacitor application, Sci. Total Environ. 871 (2023) 162045, https://doi.org/10.1016/j.scitotenv.2023.162045.
[20] C. Wang, H. Wang, B. Dang, Z. Wang, X. Shen, C. Li, Q. Sun, Ultrahigh yield of nitrogen doped porous carbon from biomass waste for supercapacitor, Renew. Energy 156 (2020) 370–376, https://doi.org/10.1016/j.renene.2020.04.092.
[21] J. Huang, S. Zhu, J. Zhang, G. Han, One-pot ultrafast molten-salt synthesis of anthracite-based porous carbon for high-performance capacitive energy storage, ACS Materials Lett. 6 (2024) 2144–2152, https://doi.org/10.1021/acsmaterialslett.4c00275.
[22] L. Luo, Y. Lan, Q. Zhang, J. Deng, L. Luo, Q. Zeng, H. Gao, W. Zhao, A review on biomass-derived activated carbon as electrode materials for energy storage supercapacitors, J. Energy Storage. 55 (2022) 105839, https://doi.org/10.1016/j.est.2022.105839.
[23] J. Zhao, Y. Jiang, H. Fan, M. Liu, O. Zhuo, X. Wang, Q. Wu, L. Yang, Y. Ma, Z. Hu, Porous 3d few-layer graphene-like carbon for ultrahigh-power supercapacitors with well-defined structure–performance relationship, Adv. Mater. 29 (2017) 1604569, https://doi.org/10.1002/adma.201604569.
[24] P. Han, M. Cheng, D. Luo, W. Cui, H. Liu, J. Du, M. Wang, Y. Zhao, L. Chen, C. Zhu, J. Xu, Selective etching of c-n bonds for preparation of porous carbon with ultrahigh specific surface area and superior capacitive performance, Energy Storage Mater. 24 (2020) 486–494, https://doi.org/10.1016/j.ensm.2019.07.009.
[25] Y. Tang, X. Wang, J. Chen, D. Wang, Z. Mao, Synthesis of presodiated b, n co-doped carbon materials and application in sodium ions batteries with enhanced initial coulombic efficiency, Chem. Eng. J. 427 (2022) 131951, https://doi.org/10.1016/j.cej.2021.131951.
[26] Q. Wang, J. Yan, Z. Fan, Carbon materials for high volumetric performance supercapacitors: design, progress, challenges and opportunities, Energy Environ. Sci. 9 (2016) 729–762, https://doi.org/10.1039/c5ee03109e.
[27] F. Wei, X. He, L. Ma, H. Zhang, N. Xiao, J. Qiu, 3D n,o-codoped egg-box-like carbons with tuned channels for high areal capacitance supercapacitors, Nano-Micro Lett. 12 (2020), https://doi.org/10.1007/s40820-020-00416-2.
[28] P. Wang, X. Qi, W. Zhao, M. Qian, H. Bi, F. Huang, Nitrogen-doped hierarchical few-layered porous carbon for efficient electrochemical energy storage, Carbon Energy 3 (2020) 349–359, https://doi.org/10.1002/cey2.78.
[29] J. Lee, C. Kim, J.Y. Cheong, I.-D. Kim, An angstrom-level d-spacing control of graphite oxide using organofillers for high-rate lithium storage, Chem 8 (2022) 2393–2409, https://doi.org/10.1016/j.chempr.2022.05.002.
[30] S. Lu, M. Jin, Y. Zhang, Y. Niu, J. Gao, C. Li, Chemically exfoliating biomass into a graphene-like porous active carbon with rational pore structure, good conductivity, and large surface area for high-performance supercapacitors, Adv. Energy Mater. 8 (2017) 1702545, https://doi.org/10.1002/aenm.201702545.

[31] U. Bhattacharjee, S. Bhowmik, S. Ghosh, N. Vangapally, S.K. Martha, Boron-doped graphene anode coupled with microporous activated carbon cathode for lithium-ion ultracapacitors, Chem. Eng. J. 430 (2022) 132835, https://doi.org/10.1016/j.cej.2021.132835.
[32] H. Wang, J. Deng, C. Xu, Y. Chen, F. Xu, J. Wang, Y. Wang, Ultramicroporous carbon cloth for flexible energy storage with high areal capacitance, Energy Storage Mater. 7 (2017) 216–221, https://doi.org/10.1016/j.ensm.2017.03.002.
[33] X. Xiang, Z. Deng, H. Zhang, C. Gao, S. Feng, Z. Liu, Q. Liang, Y. Fu, Y. Liu, K. Liu, Polyaniline/polydopamine-regulated nitrogen-doped graphene aerogel with well-developed mesoporous structure for supercapacitor electrode, Chem. Eng. J. 477 (2023) 147211, https://doi.org/10.1016/j.cej.2023.147211.
[34] N. Yang, S. Yu, W. Zhang, H.M. Cheng, P. Simon, X. Jiang, Electrochemical capacitors with confined redox electrolytes and porous electrodes, Adv. Mater. 34 (2022), https://doi.org/10.1002/adma.202202380.
[35] Y. Qi, B. Ge, Y. Zhang, B. Jiang, C. Wang, M. Akram, X. Xu, Three-dimensional porous graphene-like biochar derived from enteromorpha as a persulfate activator for sulfamethoxazole degradation: role of graphitic n and radicals transformation, J. Hazard. Mater. 399 (2020) 123039, https://doi.org/10.1016/j.jhazmat.2020.123039.
[36] Z. Ling, Z. Wang, M. Zhang, C. Yu, G. Wang, Y. Dong, S. Liu, Y. Wang, J. Qiu, Sustainable synthesis and assembly of biomass-derived b/n co-doped carbon nanosheets with ultrahigh aspect ratio for high-performance supercapacitors, Adv. Funct. Mater. 26 (2015) 111–119, https://doi.org/10.1002/adfm.201504004.
[37] Y. Li, Z. Li, P.K. Shen, Simultaneous formation of ultrahigh surface area and three-dimensional hierarchical porous graphene-like networks for fast and highly stable supercapacitors, Adv. Mater. 25 (2013) 2474–2480, https://doi.org/10.1002/adma.201205332.
[38] W. Wei, K. Sun, Y.H. Hu, Synthesis of 3d cauliflower-fungus-like graphene from co2as a highly efficient counter electrode material for dye-sensitized solar cells, J. Mater. Chem. A 2 (2014) 16842–16846, https://doi.org/10.1039/c4ta03909b.
[39] E. Zhang, Y. Wu, H. Shao, V. Klimavicius, H. Zhang, P.-L. Taberna, J. Grothe, G. Buntkowsky, F. Xu, P. Simon, S. Kaskel, Unraveling the capacitive charge storage mechanism of nitrogen-doped porous carbons by eqcm and ssnmr, J. Am. Chem. Soc. 144 (2022) 14217–14225, https://doi.org/10.1021/jacs.2c04841.
[40] I. Lamata-Bermejo, W. Keil, K. Nolkemper, J. Heske, J. Kossmann, H. Elgabarty, M. Wortmann, M. Chorążewski, C. Schmidt, T.D. Kühne, N. López-Salas, M. Odziomek, Understanding the wettability of C1N1 (sub)nanopores: implications for porous carbonaceous electrodes, Angew. Chem. Int. Ed. 63 (2024) e202411493, https://doi.org/10.1002/anie.202411493.
[41] C. Leng, Z. Zhao, Y. Song, L. Sun, Z. Fan, Y. Yang, X. Liu, X. Wang, J. Qiu, 3d carbon frameworks for ultrafast charge/discharge rate supercapacitors with high energy-power density, Nano-Micro Lett. 13 (2020), https://doi.org/10.1007/s40820-020-00535-w.
[42] J. Li, P.J. Burke, Measurement of the combined quantum and electrochemical capacitance of a carbon nanotube, Nat. Commun. 10 (2019), https://doi.org/10.1038/s41467-019-11589-9.
[43] Q. Wang, F. Liu, Z. Jin, X. Qiao, H. Huang, X. Chu, D. Xiong, H. Zhang, Y. Liu, W. Yang, Hierarchically divacancy defect building dual-activated porous carbon fibers for high-performance energy-storage devices, Adv. Funct. Mater. 30 (2020) 2002580, https://doi.org/10.1002/adfm.202002580.
[44] X. Ma, P. Miao, B. Zhang, Y. Wang, Q. Guo, Z. Su, G. Hu, H. Wang, G. Jin, Cotton induced graphene-like carbon tubes as electrodes for ultrahigh-energy–density supercapacitors, Chem. Eng. J. 495 (2024) 153229, https://doi.org/10.1016/j.cej.2024.153229.
[45] W.J.S. Siow, J.Y. Chong, J.H. Ong, M. Kraft, R. Wang, R. Xu, Vapor/vapor-solid interfacial growth of covalent organic framework membranes on alumina hollow fiber for advanced molecular separation, Angew. Chem. Int. Ed. 63 (2024), https://doi.org/10.1002/anie.202406830.
[46] S. Cai, R. Ma, W. Ke, H. Zhang, Y. Liu, M. Jiao, Y. Tian, Y. Fang, M. Wu, Z. Zhou, Flower-like covalent organic frameworks as host materials for high-performance lithium-sulfur batteries, Chem. Eng. J. 491 (2024) 151979, https://doi.org/10.1016/j.cej.2024.151979.
[47] J. Tian, C. Cui, Q. Xie, W. Qian, C. Xue, Y. Miao, Y. Jin, G. Zhang, B. Guo, $EMIMBF_4$–gbl binary electrolyte working at −70 °C and 3.7 V for a high performance graphene-based capacitor, J. Mater. Chem. A 6 (2018) 3593–3601, https://doi.org/10.1039/c7ta10474j.
[48] S. Feng, Q. Zhao, J. Wang, W. Zhang, W. Wang, M. Xu, L. Zhou, L. Mai, D. Zhao, Y. Liu, High capacitance based on vacancy defective porous carbon in ionic liquid, Adv. Funct. Mater. 34 (2024), https://doi.org/10.1002/adfm.202401045.
[49] D. Sui, R. Luo, Shumin Xie, Heng Zhang, Tiantian Ma, Hao Sun, Tong-Tong Jia, Jing Sun, Xingyun Li, Atomic ruthenium doping in collaboration with oxygen vacancy engineering boosts the hydrogen evolution reaction by optimizing H absorption, Chem. Eng. J. 480 (2024) 148007, https://doi.org/10.1016/j.cej.2023.148007.

Supporting Information

Revealing the "Double-layer Ionic Monotonic Adsorption" Electrochemical Ion Storage Mechanism of Nano-confined Porous Carbon

Gaojie Li[1‡], Xinbo Guo[1‡], Yu Liu[1], Jianguo Sun[3], Hang Yang[2], Yang Zheng[1], Xuming Zhang[1], Paul K. Chu[4], Guanjie He[2]*, and Biao Gao[1]**

[1]*The State Key Laboratory of Advanced Refractories, Wuhan University of Science and Technology, Wuhan 430081, China*

[2]*Christopher Ingold Laboratory, Department of Chemistry, University College London, 20 Gordon Street, London, WC1H 0AJ, UK.*

[3]*Department of Materials Science and Engineering, National University of Singapore, Singapore 117574, Singapore*

[4]*Department of Physics, Department of Materials Science and Engineering, and Department of Biomedical Engineering, City University of Hong Kong, Tat Chee Avenue, Hong Kong, China*

‡ *These authors contributed equally to this work*

**Corresponding author. E-mail: liuyu_lab@163.com; g.he@ucl.ac.uk; gaobiao@wust.edu.cn*

Experimental section

Preparation of 3DPFC

The obtained 3DPFC were directly synthesized from biocarbon through a low-temperature salt activation method. Firstly, coconut shells were pulverized below 50 μm by jet mill and then carbonized at 600 °C for 3 h under an N_2 atmosphere to produce biocarbon after natural cooling to room temperature. Next, the biocarbon powders were mixed with salt at a weight ratio of 1 : 4 followed by heated up to different temperatures (850 °C, 900 °C, 950 °C) for 5 h at a rate of 10 °C min^{-1} under a nitrogen atmosphere after natural cooling to room temperature (Fig. S1a). Among, 50 g biocarbon powders 105 g K_2CO_3 and 95 g Na_2CO_3 (The molar ratio of K_2CO_3 : Na_2CO_3 is 0.45:0.55) are mixed through an agate mortar (Fig. S1b-c). The products were washed with 10 wt% hydrochloric acid solution and deionized water until neutral pH, and finally dried by vacuum drying oven at 100 °C for 12 h (Fig. S1d). The final products were recorded as 3DPFC-850, 3DPFC-900, and 3DPFC-950, respectively.

Density Functional Theory

Theoretical calculation method: The density functional theory (DFT) method of the Dmol3 module was used with the GGA/PBE functional, custom Grimme DFT-D parameters, and DNP 4.4 basis set in Material Studio 2020. The generalized gradient approximation (GGA) with the Perdew, Burke, and Ernzerhof (PBE) exchange-correlation energy was employed. The convergence of energy, forces, and maximum displacement were set to 1×10^{-5} Ha, 0.002 Ha/Å and 5.0×10^{-3} Å, respectively. Gamma 1×1×1 k-points were used to sample the Brillouin zone. Crystal structure diagrams were drawn with Visualization for Electronical and Structural Analysis (VESTA). The binding energy (EB) of the ion group is defined by the following equation:

$$EB=E_{Total}-E_1-E_2 \quad (1)$$

Where E_{Total} is the total energy of molecule-composite, E_1 and E_2 are the energies of molecule-1 and molecule-2, respectively.

Structure characterization

The surface morphology of samples was characterized by scanning electron microscopy (SEM, Hitachi S-4800, operating at 10 kV), transmission electron microscope (TEM, JEOL E-2100), and high-resolution transmission electron microscopy (HR-TEM, JEM-2100F). X-ray diffraction (XRD) patterns were obtained from an X-ray powder diffraction (Smart Lab SE) using Cu Kα radiation (λ = 0.15406 nm). Raman spectra were performed by a 532 nm laser (Horiba HR revolution) with Raman spectroscopy. X-ray photoelectron spectroscopy (XPS) was performed with a VG Microtech ESCA 2000 using a monochromic Al X-ray source (AXIS SUPRA+, Kratos). The porous structures and specific surface area of the samples were measured by N2 adsorption-desorption at 77.3 K (Quadrasorb SI-MP device, ASAP2020). The specific surface area of the samples was calculated based on the Braunauer-Emmett-Teller (BET) method. The pore volume and pore size distribution were determined by the density functional theory (DFT) method. The electrical conductivity was tested by powder resistivity & compaction density measurement system (PRCD3110) at different pressures.

Electrochemical measurements

The electrochemical properties were carried out by an electrochemical workstation (CHI 760e) and electrochemical test system. The cycling voltammetry (CV) and galvanostatic charge/discharge (GCD) were tested by an electrochemical workstation (CHI 760e, Shanghai Chenhua Instruments Co., China). Electrochemical impedance spectroscopy (EIS) was performed with an electrochemical workstation in a frequency range of 100 kHz to 10 MHz.

For the Three-Electrode System: the working electrodes were fabricated by mixing 90 wt% of 3DPFC and 10 wt% of polytetrafluoroethylene (PTFE) binder. The mixture was uniformly blended completely, rolled into a thin film, and punched into circular sheets with an area of about 1.12 cm^2. The circular sheets were dried under vacuum at 120 °C for 12 h and then pasted on a nickel foam current collector at 10 Mpa for 20 s, resulting in 2-3 mg cm^{-2} of mass loading. For the standard three-electrode system, Hg/HgO electrode and platinum plate were used as reference electrodes and counter electrodes, respectively, using a 6M KOH electrolyte. The gravimetric specific

capacitance of a single electrode was calculated by using the following equations:

$$C_g = \frac{I\,\Delta t}{m\Delta V} \qquad (1)$$

where I, Δ t, m, and Δ V are the constant current (mA), discharging time (s), the mass of one electrode in a three-electrode system and both electrodes in a two-electrode system (mg), and the operating voltage (V), respectively.

For the two-electrode system: The cell was composed of symmetrical electrode materials. The single electrode mass was about 2-3.5 mg cm^{-2} in 6 M KOH and [EMIM][BF_4]/PC when 3DPFC were used as the electrode. The ionic liquid electrolyte was assembled with a CR2032 coin cell battery, the separator was TF-40 with a diameter of 16 mm, and copper foil as the current collector. Moreover, the energy density (E, Wh kg^{-1}) and power density (P, W kg^{-1}) of the coin cell type supercapacitor were calculated by the following equations:

$$C_1 = \frac{2I\,\Delta t}{m\Delta V} \qquad (2)$$

$$E = \frac{C\,\Delta V^2}{2*3.6} \qquad (4)$$

$$P = \frac{3600E}{\Delta t} \qquad (5)$$

Where C is the specific capacitance of the sample in the two-electrode cell, V is the set voltage window (V)

In-situ Raman Spectroscopy Analysis: For in situ Raman spectroscopy, a 3DPFC-900 electrode was obtained using a mixture of 3DPFC-900 and PVDF, in a weight ratio of 9:1. Other conditions for assembling in-situ cells are the same as for coin cells. The cell was continuously charged/discharged at a current density of 0.5 A g^{-1} during the collection process of Raman spectra through a quartz window.

In-situ ATR-FTIR measurement: Infrared experiments were obtained on an FT-IR spectrometer (Nicolet iS50, Thermo Scientific) instrument with an MCT-A detector. The bottom of the electrochemical cell was constructed using a ZnSe prism beveled at 60°. The spectra were acquired in external reflection using a liquid-N_2-cooled MCT (mercury−cadmium−telluride) detector. The working electrode (3DPFC-900) was placed on the back of the ZnSe wedge window, with another 3DPFC-900 electrode

serving as the counter electrode. The spectra were recorded at intervals of 60 s over the 500−2500 cm^{-1} range, with a resolution of 4 cm^{-1} and an interferometer frequency of 40 kHz.

Fig. S1. a) Photos of the preparation workshop equipment. b) Photos of the mixed material before activation. c) Photos of the materials after activation. d) Photos of the final product.

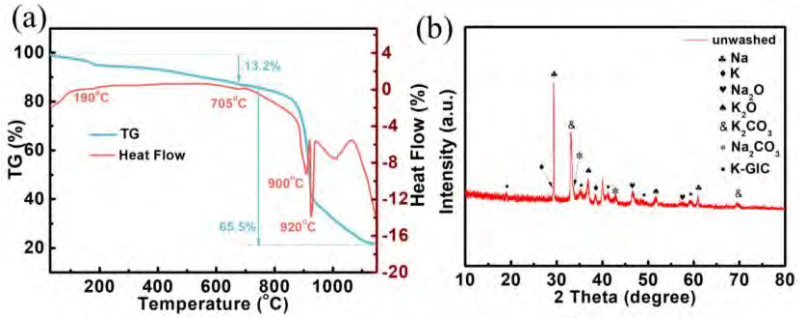

Fig. S2. a) TG curves and differential thermogravimetric curves of 3DPFC. b) XRD patterns of 3DPFC-900.

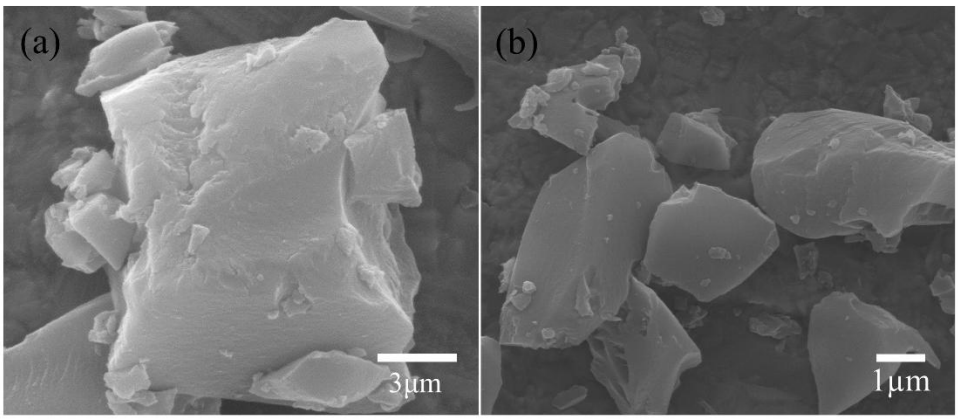

Fig. S3. SEM images of biocarbon.

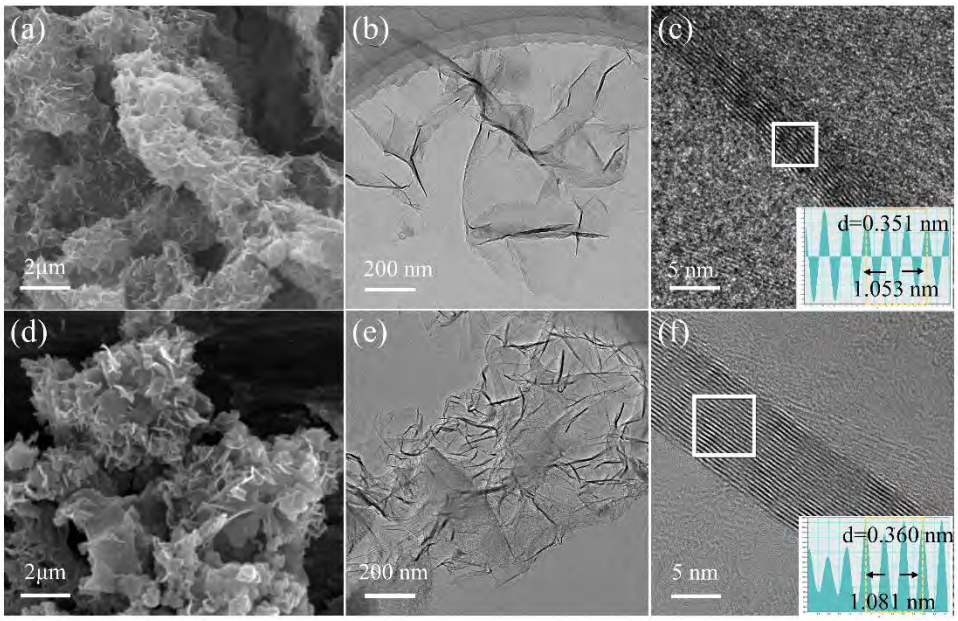

Fig. S4. a) SEM images of 3DPFC-850. b) TEM images of 3DPFC-850. c) High-resolution TEM images of 3DPFC-850. d) SEM images of 3DPFC-950. e) TEM images of 3DPFC-950. f) High-resolution TEM images of 3DPFC-950.

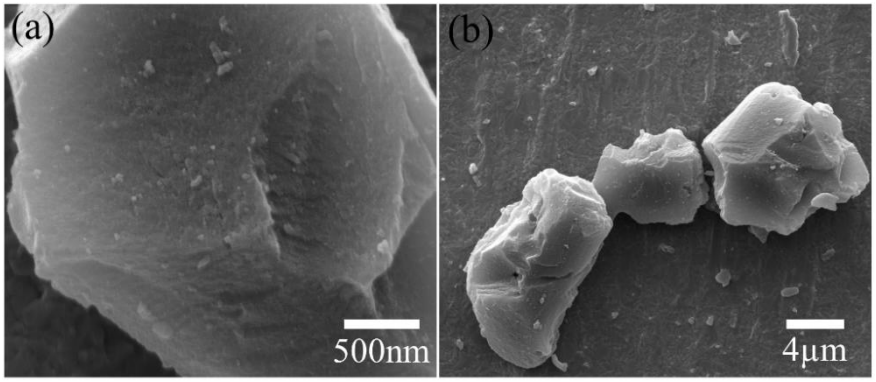

Fig. S5. SEM images of YP-50F.

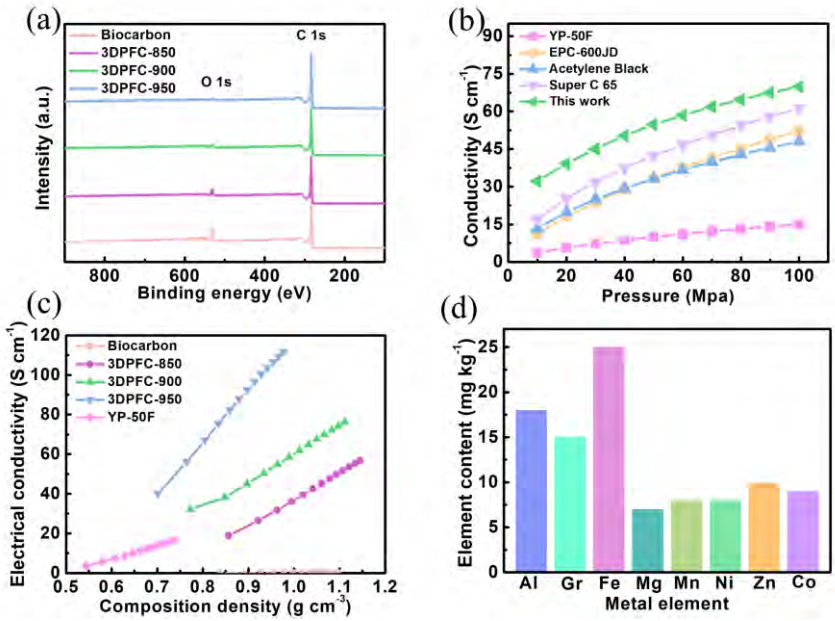

Fig. S6. a) The XPS survey spectra of all samples. b) Conductivity comparison. c) Electrical conductivity as a function of composition density. d) Metal element content of 3DPFC-900.

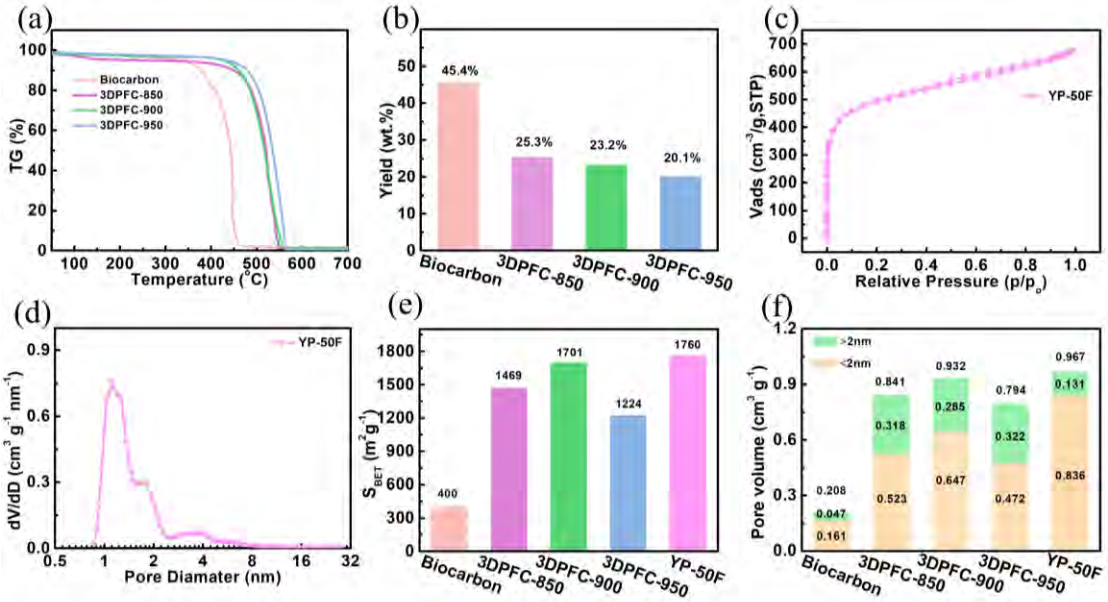

Fig. S7. a) TG curve of the sample in the air environment. b) Yield of finished carbon. c) N_2 adsorption/desorption curve of YP-50F. d) Pore size distribution of YP-50F. e) Specific surface area of the sample. f) Pore volume of the sample.

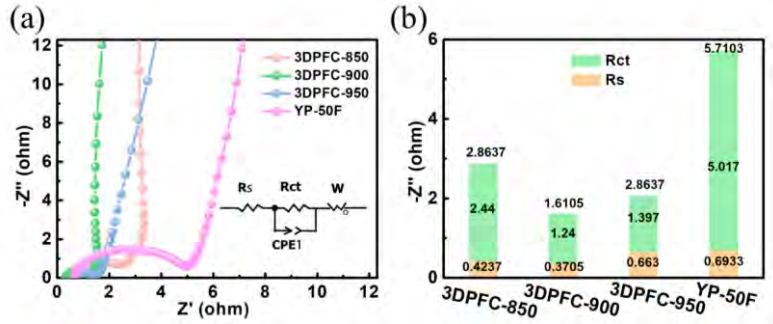

Fig. S8. a) Nyquist plots of 3DPFC and YP-50F in three-electrode system. b) The equivalent circuit fits the impedance value of 3DPFC and YP-50F.

The capacitive performances of all samples were tested by the three-electrode system in 6 M KOH at room temperature. The 3DPFC electrode possesses a smaller semicircle and more vertical line than YP-50F and biocarbon, implying a smaller charge-transfer resistance and better capacitive behavior (Fig. S8).

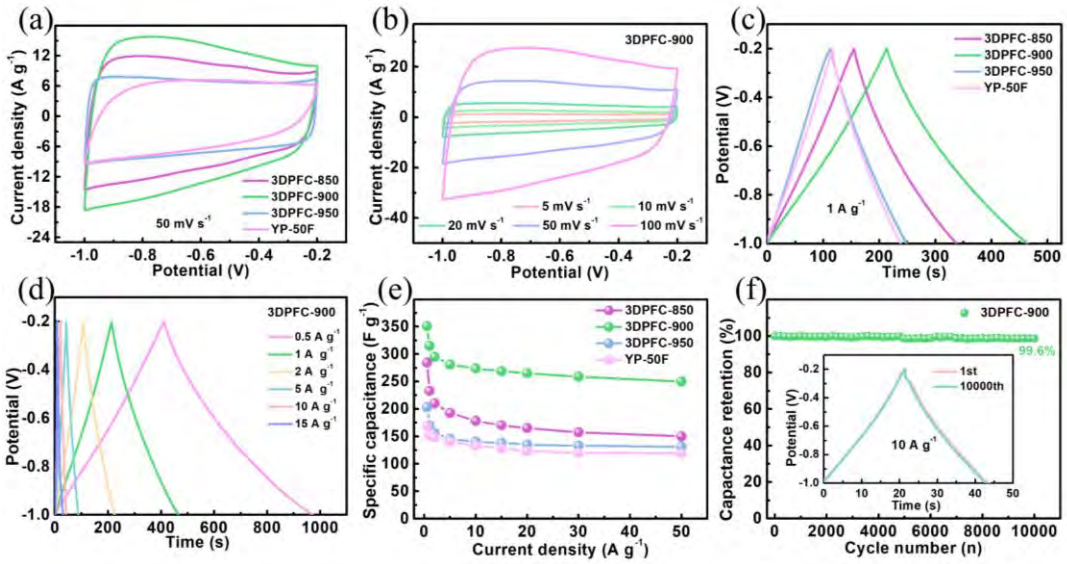

Fig. S9. The electrochemical properties of YP-50F and 3DPFC in a three-electrode system. a) CV curves of YP-50F and 3DPFC at 50 mV s^{-1}. b) CV curves of 3DPFC-900 from 5-100 mV s^{-1}. c) GCD curves of YP-50F and 3DPFC at 1 A g^{-1}. d) GCD curves of 3DPFC-900 at different current densities. e) Rate performance of YP-50F and 3DPFC. f) Cycling stability of 3DPFC-900 at 10 A g^{-1}.

The CV curves of all samples are approximate rectangular shapes at 50 mV s^{-1} as

shown in Fig. S9a, suggesting a typical characteristic of the electric double-layer capacitance (EDLC). At the same time, 3DPFC-900 shows the largest rectangular area, implying the largest specific capacitance among all samples. Notably, even at 100 mV s^{-1}, the 3DPFC-900 still keeps a well-rectangular shape, indicating a fast charge transfer rate and superior rate characteristic (Fig. S9b). Furthermore, the GCD curves of all samples show a triangle shape at 1 A g^{-1}, and 3DPFC-900 shows the maximum charge-discharge times (Fig. S9c), which means the maximum specific capacitance that is consistent with the CV result (maximum CV area). Interestingly, the specific capacitance of 3DPFC-900 is 314 F g^{-1}, which is higher than that of the YP-50F (152 F g^{-1}). In addition, the specific capacitance of the obtained 3DPFC-900 electrode is significantly higher than that of many reported biomass-derived porous graphene carbonaceous materials [1, 2]. The GCD profiles of 3DPFC-900 exhibit an almost symmetrical triangle shape at different current densities, indicating excellent capacitor behavior and favorable electrochemical reversibility (Fig. S9d). Even at current densities of 50 A g^{-1}, the capacitance value of the 3DPFC-900 electrode is 250 F g^{-1} corresponding to 71.4% retention (Fig. S9e). In addition, the 3DPFC-900 electrode can maintain 99.5% of the initial specific capacitance after 10,000 cycles at the high current density of 10 A g^{-1} (Fig. S9f). Such high cycling stability can be attributed to its layered open porous structure, which avoids π-π aggregation and restacking of graphene-like sheets and can accommodate the deformation of the framework.

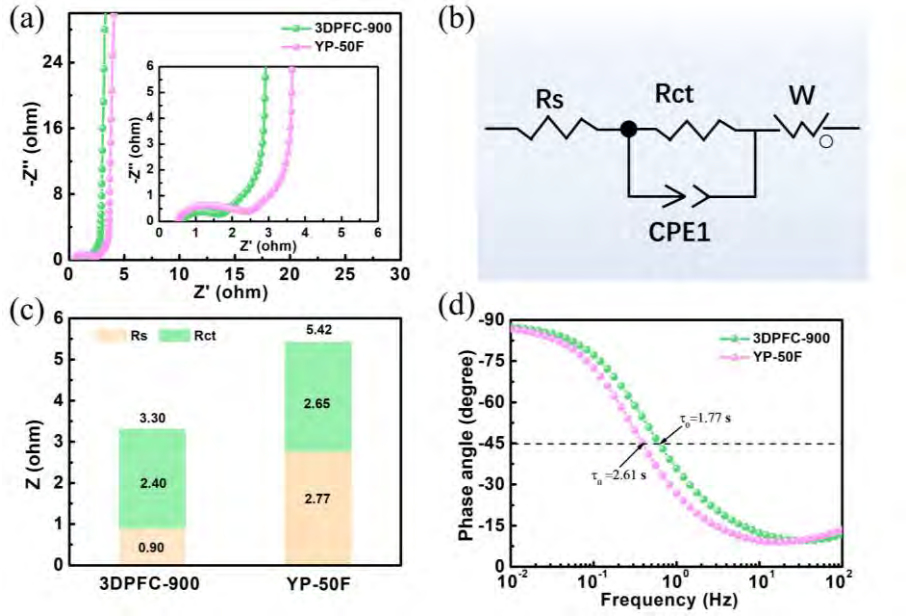

Fig. S10. a) Nyquist plots of YP-50F and 3DPFC-900 in two-electrode system. b) Equivalent circuit. c) The equivalent circuit fits the impedance values of YP-50F and 3DPFC-900. d) Bode plots of YP-50F and 3DPFC-900.

To examine the electrochemical performance of 3DPFC-900 for practical application, the supercapacitor with 3DPFC-900 as the symmetric electrodes (denoted as 3DPFC-900//3DPFC-900) was fabricated with the 6 M KOH as the electrolyte. For the Nyquist plot of the 3DPFC-900 in KOH electrolyte, it can be seen that the straight part in the low-frequency region is well vertical, while the smaller semicircle in the high-frequency region represents a small Warburg impedance (Fig. S10a-10c). Such a phenomenon confirms both the typical characteristics of a double electric layer capacitor and the fast ion diffusion. In particular, 3DPFC-900 exhibits the lowest resistance, suggesting its fastest ion and electron transport kinetics. Bode plots show that the relaxation time constant τ_0 ($\tau_0 = 1/f_0$, f_0 is the characteristic frequency of the phase angle of -45°) of YP-50F and 3DPFC-900 are 2.61 s and 1.77 s, respectively, identifying the best charge/discharge rate of 3DPFC-900 ascribed to their largest ion-accessible surface area and suitable pore distribution (Fig. S10d).

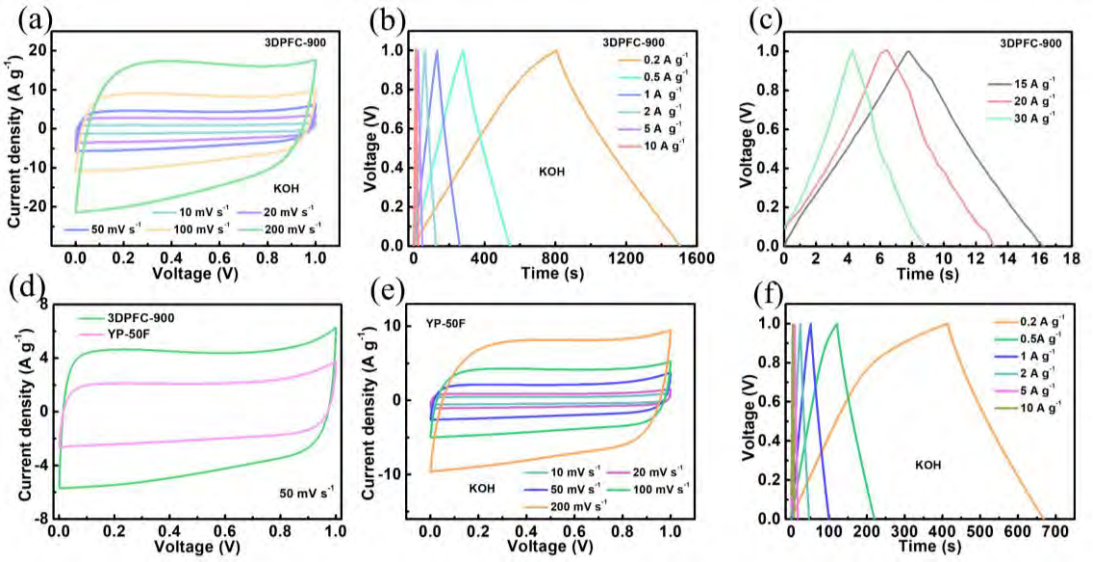

Fig. S11. The electrochemical properties of 3DPFC-900 and YP-50F based supercapacitors in 6 M KOH electrolyte. a) CV curves of 3DPFC-900 capacitors from 10-200 mV s^{-1}. b, c) GCD curves of 3DPFC-900 capacitors. d) CV curves of 3DPFC-900 and YP-50F capacitors at 50 mV s^{-1}. e) CV curves of YP-50F capacitors from 10-200 mV s^{-1}. f) GCD curves of YP-50F capacitors.

To examine the electrochemical performance of 3DPFC-900 for practical application, the supercapacitor with 3DPFC-900 as the symmetric electrodes (denoted as 3DPFC-900//3DPFC-900) was fabricated with the 6 M KOH as the electrolyte. The GCD curves of the symmetric 3DPFC-900 supercapacitor presented a perfect equilateral triangle shape from 0.2 to 30 A g^{-1}, which is much better than that of YP-50F (Fig. S11b-c and Fig. S11e-f).

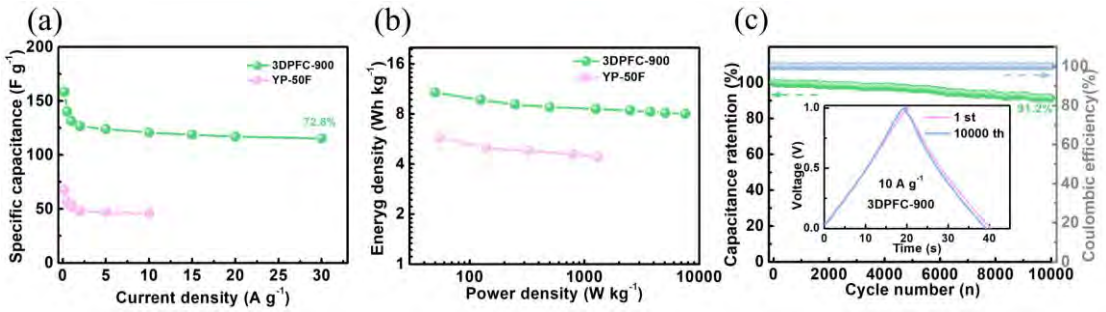

Fig. S12. The electrochemical properties of 3DPFC-900 and YP-50F based supercapacitors in 6 M KOH electrolyte. a) Rate performance of 3DPFC-900 and YP-50F capacitors. b) Ragone plots of 3DPFC-900 and YP-50F capacitors. c) Cycling stability of 3DPFC-900 capacitor at 10 A g^{-1}.

The specific capacitance of 3DPFC-900 capacitors is calculated to 158.5 and 120.9 F g^{-1} at 0.2 and 10 A g^{-1} as shown in Fig. S12a. The capacitance of the symmetric 3DPFC-900 capacitor still maintains 72.8% at the high current density of 30 A g^{-1}, which exhibits outstanding rate performance. In Fig. S12b, the Ragone plots clearly show that the 3DPFC-900-based supercapacitors deliver an energy density of 10.8 Wh kg^{-1} at a power density of 50 W kg^{-1} in KOH electrolyte, which is superior to the YP-50F capacitors with the energy density of 5.8 Wh kg^{-1} at a power density of 54 W kg^{-1}. Such performance of the 3DPFC-900 based symmetric supercapacitor is better or no worse than some previously reported carbon-based materials (Table S3). In addition, long cycling testing shows that the 3DPFC-900 supercapacitor still possesses 91.53% capacitance and 100% Coulomb efficiency after 10,000 cycles at 10 A g^{-1}, demonstrating much higher cycling stability (Fig. 12c).

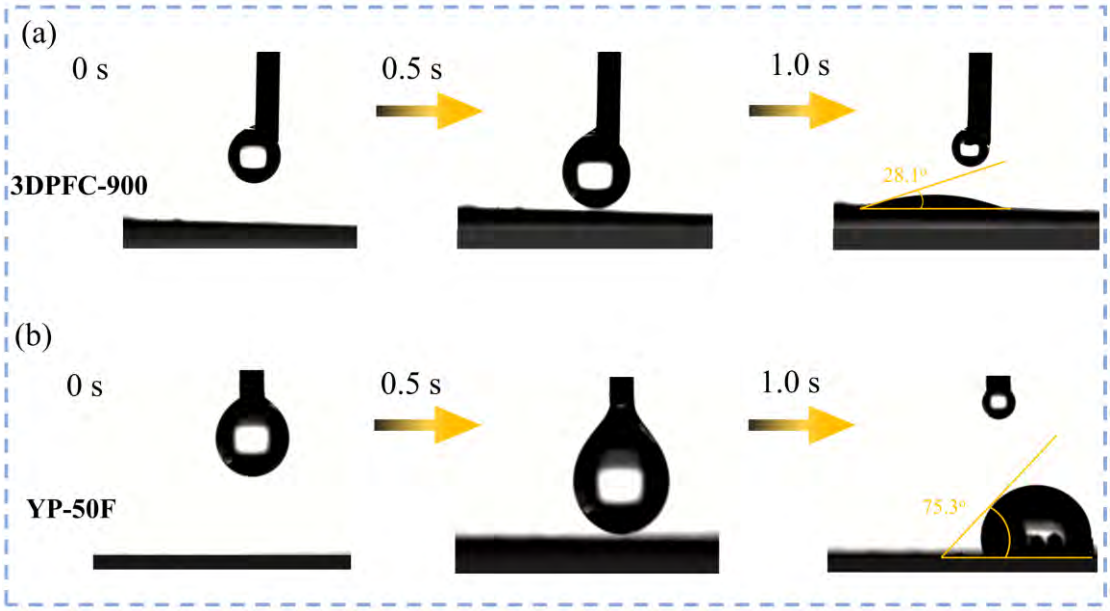

Fig. S13. Contact angle testing of 3DPFC-900 and YP-50F in [EMIM][BF_4]/PC electrolyte.

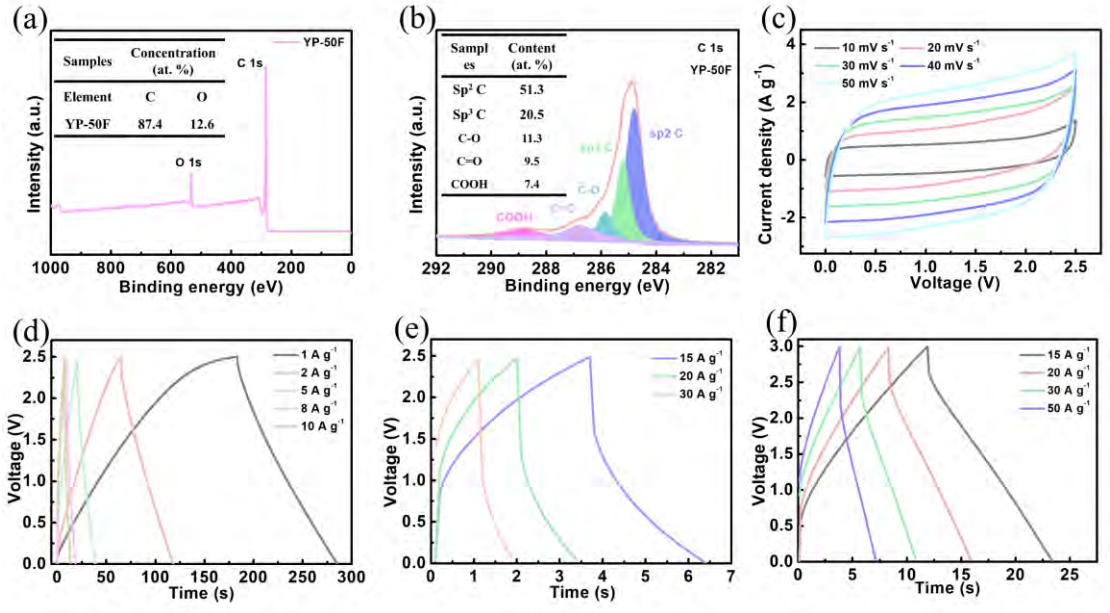

Fig. S14. a, b) Survey spectrum and C 1s of YP-50F. c-e) CV curves and GCD curves of YP-50F capacitors in [EMIM][BF_4]/PC. f) GCD curves of 3DPFC-900 capacitors in [EMIM][BF_4]/PC.

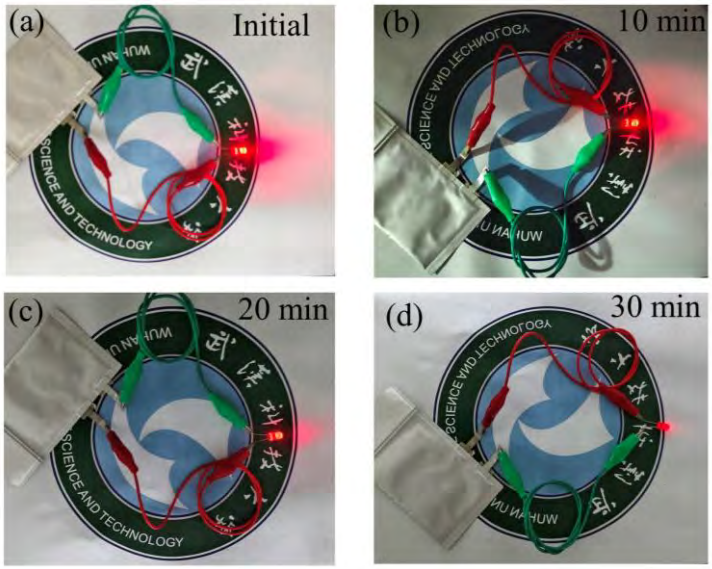

Fig. S15. LED discharge time for 3DPFC-900 capacitors.

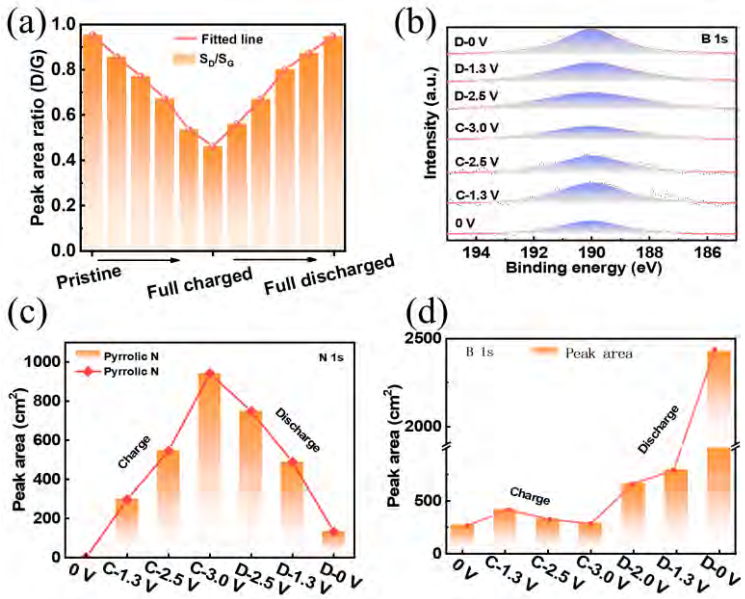

Fig. S16. a) Variation of S_D/S_G value with the voltage. b) *Ex situ* XPS spectra of B 1s for negative electrode at a different voltage. c) Peak area of Pyrrolic N at different voltage states. d) Peak area of B 1s at different voltage states.

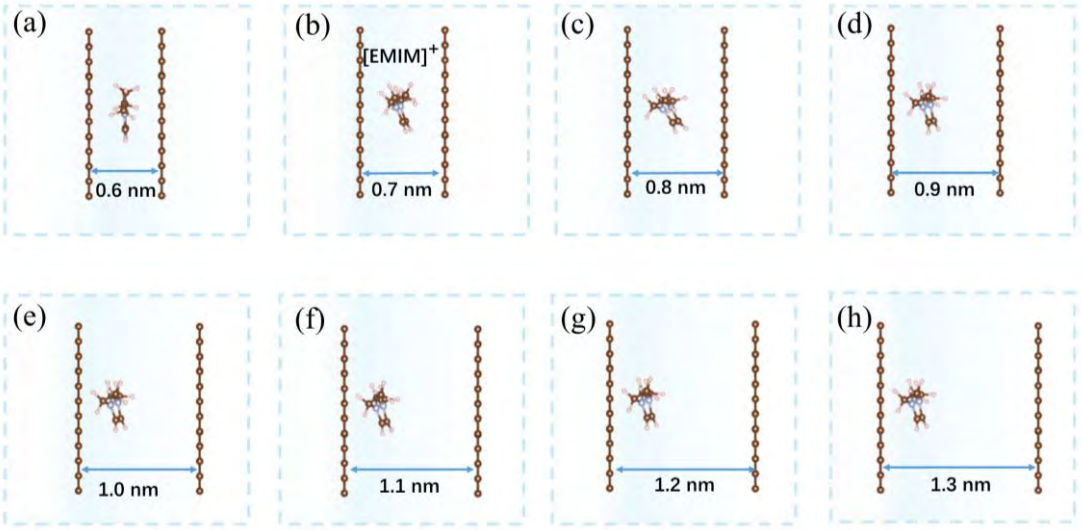

Fig. S17. Adsorption models of single $[EMIM]^+$ in carbon pores with a pore size of a) 0.6 nm, b) 0.7 nm, c) 0.8 nm, d) 0.9 nm, e) 1.0 nm, f) 1.1 nm, g) 1.2 nm, h) 1.3 nm.

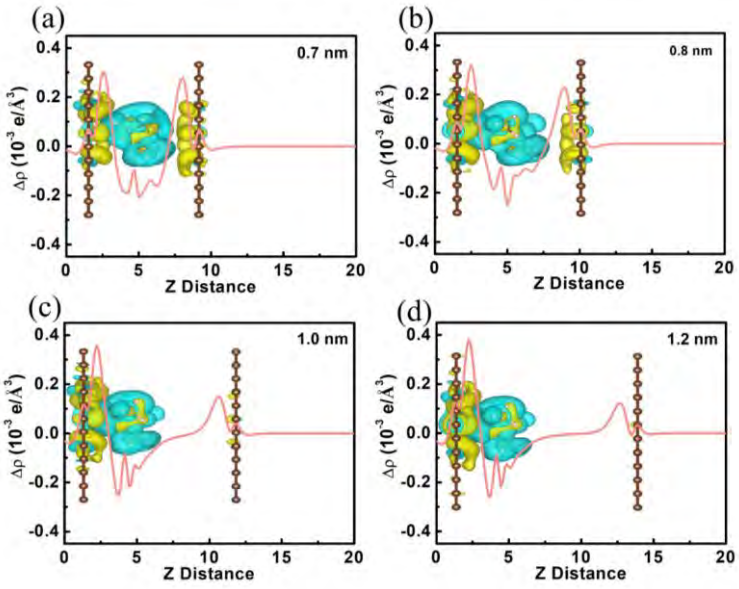

Fig. S18. The planar average charge density difference of single $[EMIM]^+$ adsorbed in carbon pores with a pore size of a) 0.7 nm, b) 0.8 nm, c) 1.0 nm, d) 1.2 nm.

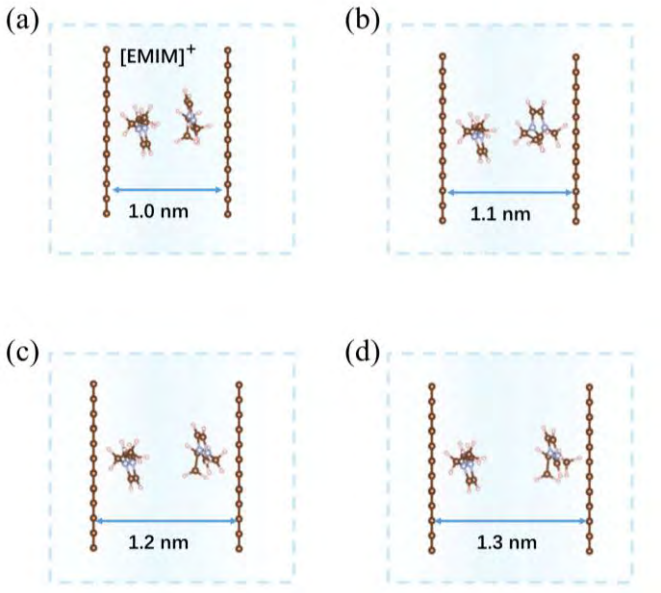

Fig. S19. Adsorption models of two $[EMIM]^+$ on carbon pores with a pore size of a) 1.0 nm, b) 1.1 nm, c) 1.2 nm, d) 1.3 nm.

Table S1. Concentration of carbon and oxygen in the samples from XPS survey spectra, and contribution of the components in the area of the XPS C 1s spectra.

Samples name	**Concentration (at. %)**		**Contribution of the components in C1s spectra (%)**			
Samples	**C**	**O**	**sp^2C**	**sp^3C**	**C-O**	**C=O**
Biocarbon	81.4	18.6	45.74	33.18	9.13	11.95
3DPFC-850	88.2	11.8	65.37	20.43	6.26	7.94
3DPFC-900	95.2	4.8	70.13	18.16.	5.06	6.65
3DPFC-950	96.7	3.3	75.67	16.06	3.18	5.09

Table S2. Specific surface area and pore size parameters of samples based on the adsorption curves.

Samples	BET ($m^2 g^{-1}$)		Pore volume ($cm^3 g^{-1}$)		D_{avg} (nm)
	Total	Micro	Micro	Total	
Biocarbon	400	350	0.161	0.208	0.478
3DPFC-850	1469	890	0.523	0.841	0.802
3DPFC-900	1701	1205	0.647	0.932	0.924
3DPFC-950	1224	835	0.472	0.794	1.173
YP-50F	1760	1416	0.536	0.967	0.571

BET: Specific surface area determined according to BET method
avg: Average pore diameter

Table S3. The comparison of 3DPFC-900 with other reported carbon materials in a two-electrode system (6M KOH).

Materials reported	**Electrolyte**	**System**	**C_{cell} (F g^{-1})**	**Rate performance (%)**	**E (Wh kg^{-1})**	**P (kW kg^{-1})**	**Ref.**
HMCSs from SiO_2@C/SiO_2	6 M KOH	Two-electrode	-	-	9.6	0.125	[3]
ACWS-6 from walnut shell	6 M KOH	Two-electrode	82.5 (1 A/g)	81% (0.5 ~ 100 A/g)	10.2	0.025	[4]
PLC-Zn from lignin	6 M KOH	Two-electrode	39 (0.2 A/g)	89.7% (0.2 ~ 10 A/g)	5.42	0.051	[5]
RCA from BAS	6 M KOH	Two-electrode	130 (0.5 A/g)	56% (0.5 ~ 10 A/g)	9.09	0.259	[6]
OPBNP from orange peel	6 M KOH	Two-electrode	-	-	8.9	0.499	[7]
N-C-HPCS from nitrocellulose	6 M KOH	Two-electrode	75 (1 A/g)	-	10.1	0.25	[8]
AC from cilantro plants	6 M KOH	Two-electrode	31.4 (0.1 A/g)	-	4.36	0.243	[9]
3DPFC-900 from coconut shell	6 M KOH	Two-electrode	158.5 (0.2 A/g)	72.8% (0.1 ~ 30 A/g)	10.8	0.05	This work

Table S4. The comparison of 3DPFC-900 with other reported carbon materials in two-electrode system (Organic electrolyte)

Materials reported	Electrolyte	System	C_{cell} (F g^{-1})	Rate performance (%)	E (Wh kg^{-1})	P (kW kg^{-1})	Ref.
DACFs from ramie fiber	[EMIM][BF_4]	Two-electrode	38.2 (0.5 A/g)	69% (1~ 10 A/g)	61.3	0.875	[10]
HCB From MCS	1 M $TEABF_4$	Two-electrode	115.8 (0.1 A/g)	72% (1 ~ 10 A/g)	30.5	0.337	[11]
HC from hibiscus sabdariffa sticks	1 M $TEABF_4$	Two-electrode	60 (1 A/g)	74% (1 ~ 20 A/g)	28.92	0.67	[12]
CTOs from cotton	1 M $TEABF_4$	Two-electrode	150 (0.5 A/g)	86.1% (0.5 ~ 5 A/g)	64.3	0.4	[13]
BGMC from template	$TEABF_4$/AN	Two-electrode	-	-	34.4	1.75	[14]
FHWSAC-3 from wheat straw	$TEABF_4$/AN	Two-electrode	66.7 (1 A/g)	-	42.1	0.135	[15]
PCCN from coal tar pitch	[EMIM][BF_4]	Two-electrode	144 (0.5 A/g)	63% (0.5 ~ 100 A/g)	72.1	0.477	[16]
3DPFC-900 from coconut shell	[EMIM][BF_4]/PC	Two-electrode	175 (0.5 A/g)	60.5% (0.5 ~ 50 A/g)	109	0.747	This work

References

[1] B. Liu, M. Yang, D. Yang, H. Chen, H. Li, Graphene-like porous carbon nanosheets for ultra-high rate performance supercapacitors and efficient oxygen reduction electrocatalysts. J. Power Sources. 456 (2020), 227999. https://doi.org/10.1016/j.jpowsour.2020.227999

[2] L. Kong, L. Su, W. Yang, G. Shao, X. Qin, Graphene-like nitrogen-doped porous

carbon nanosheets as both cathode and anode for high energy density lithium-ion capacitor. Electrochim. Acta. 349 (2020), 136303.
https://doi.org/10.1016/j.electacta.2020.136303
[3] S. Huang, D. Ma, S. Zhai, K. Chen, W. Lai et al., Kinetics-controlled superfast co-assembly to construct hollow mesoporous carbon spheres for high-performance supercapacitors. J. Power Sources. 598 (2024), 234195.
https://doi.org/10.1016/j.jpowsour.2024.234195
[4] T. Shang, Y. Xu, P. Li, J. Han, Z. Wu et al., A bio-derived sheet-like porous carbon with thin-layer pore walls for ultrahigh-power supercapacitors. Nano Energy. 70 (2020), 104531. https://doi.org/10.1016/j.nanoen.2020.104531
[5] P. Feng, H. Wang, P. Huang, L. Zhong, S. Gan et al., Nitrogen-doped lignin-derived porous carbons for supercapacitors: Effect of nanoporous structure. Chem. Eng. J. 471 (2023), 144817. https://doi.org/10.1016/j.cej.2023.144817
[6] T. Liu, M. Yin, S. Nasir, B. Li, A. Tooba et al., Co-carbonization of bitumen asphaltenes and recycled cellulose acetate to fabricate hierarchical porous carbon with superior supercapacitor performance. Chem. Eng. J. 505 (2025), 159843.
https://doi.org/10.1016/j.cej.2025.159843
[7] Y. Li, X. Zou, S. Li, Y. Chen, G. Wang et al., Biomass-derived b/n/p co-doped porous carbons as bifunctional materials for supercapacitors and sodium-ion batteries. J. Mater. Chem. A. 12 (2024), 18324-18337. https://doi.org/10.1039/d4ta02115k
[8] S. Park, B. Seo, D. Shin, K. Kim, W. Choi, Sodium-chloride-assisted synthesis of nitrogen-doped porous carbon shells via one-step combustion waves for supercapacitor electrodes. Chem. Eng. J. 433 (2022), 134486.
https://doi.org/10.1016/j.cej.2021.134486
[9] S. Bhat, U. T. Uthappa, T. Sadhasivam, T. Altalhi, S. Soo Han et al., Abundant cilantro derived high surface area activated carbon (AC) for superior adsorption performances of cationic/anionic dyes and supercapacitor application. Chem. Eng. J. 459 (2023), 141577. https://doi.org/10.1016/j.cej.2023.141577
[10] Q. Wang, F. Liu, Z. Jin, X. Qiao, H. Huang et al., Hierarchically divacancy defect building dual-activated porous carbon fibers for high-performance energy-storage

devices. Adv. Funct. Mater. 30 (2020), 2002580.
https://doi.org/10.1002/adfm.202002580
[11] D. Zhang, W. Ma, K. Li, Manipulating internal morphology and mesoporous in monodisperse carbon nanospheres for supercapacitor with organic electrolyte. J. Energy Storage. 91 (2024), 112114. https://doi.org/10.1016/j.est.2024.112114
[12] K. Nanaji, B. V. Sarada, U. V. Varadaraju, T. N Rao, S. Anandan, A novel approach to synthesize porous graphene sheets by exploring koh as pore inducing agent as well as a catalyst for supercapacitors with ultra-fast rate capability. Renew. Energy. 172 (2021), 502-513. https://doi.org/10.1016/j.renene.2021.03.039
[13] X. Ma, P. Miao, B. Zhang, Y. Wang, Q. Guo et al., Cotton induced graphene-like carbon tubes as electrodes for ultrahigh-energy–density supercapacitors. Chem. Eng. J. 495 (2024), 153229. https://doi.org/10.1016/j.cej.2024.153229
[14] B. Cheng, B. Yang, X. Xie, L. Wan, J. Chen et al., Solvent-free mechanochemical synthesis of mg-gallic acid complex for the fabrication of high-performance supercapacitor porous carbon. Chem. Eng. J. 499 (2024), 156672.
https://doi.org/10.1016/j.cej.2024.156672
[15] Y. Li, L. Ni, J. Luo, L. Zhu, X. Zhang et al., Fenton reaction doubled biomass carbon activation efficiency for high-performance supercapacitors. Adv. Funct. Mater. 34 (2024), 2403448. https://doi.org/10.1002/adfm.202403448
[16] P. Chen, C. Lu, X. Che, B. Yan, J. Yang, 1D/2D hierarchical carbon architectures with tunable porosity for high-performance ionic liquid supercapacitors. J. Power Sources. 632 (2025), 236382. https://doi.org/10.1016/j.jpowsour.2025.236382